

Mutant SF3B1 promotes AKT and NF- κ B driven mammary tumorigenesis

Bo Liu^{1,*}, Zhaoqi Liu^{2,3,4,5,*}, Sisi Chen¹, Michelle Ki¹, Caroline Erickson¹, Jorge S. Reis-Filho⁶, Benjamin H. Durham^{1,6}, Qing Chang⁷, Elisa de Stanchina⁷, Yiwei Sun^{4,5}, Raul Rabadan^{4,5}, Omar Abdel-Wahab^{1,8,9}, Sarat Chandarlapaty^{1,9,10}

¹Human Oncology and Pathogenesis Program, Memorial Sloan Kettering Cancer Center, New York, NY, USA

²CAS Key Laboratory of Genomic and Precision Medicine, Beijing Institute of Genomics, Chinese Academy of Sciences, ³China National Center for Bioinformatics, Beijing 100101, China

⁴Program for Mathematical Genomics, ⁵Departments of Systems Biology and Biomedical Informatics, Columbia University, New York, NY, USA

⁶Department of Pathology, Memorial Sloan Kettering Cancer Center, New York, NY, USA

⁷Antitumor Assessment Core and Molecular Pharmacology Department, Memorial Sloan Kettering Cancer Center, New York, NY 10065, USA

⁸Leukemia Service, Dept. of Medicine, Memorial Sloan Kettering Cancer Center, New York, NY, USA

⁹Weill-Cornell Medicine, New York, NY, USA

¹⁰Breast Medicine Service, Dept. of Medicine, Memorial Sloan Kettering Cancer Center, New York, NY, USA

*Contributed equally

Correspondence:

Sarat Chandarlapaty

Human Oncology and Pathogenesis Program, Memorial Sloan Kettering Cancer Center, 417 East 68th Street, New York, NY 10065, USA

Office: 646-888-4311

chandars@mskcc.org

Omar Abdel-Wahab

Human Oncology and Pathogenesis Program, Memorial Sloan Kettering Cancer Center, 417 East 68th Street, New York, NY 10065, USA

Office: 646-888-3487

abdelwao@mskcc.org

CONFLICT OF INTEREST

The authors have declared that no conflict of interest exists.

DECLARATION OF INTERESTS

O.A.-W. has served as a consultant for H3B Biomedicine, Foundation Medicine Inc, Merck, and Janssen, and is on the Scientific Advisory Board of Envisagenics Inc and AIChemy; O.A.-W. has received prior research funding from H3B Biomedicine and LOXO Oncology unrelated to the current

manuscript. J.S.R.-F. reports receiving personal/consultancy fees from Goldman Sachs, Paige.AI and REPARE Therapeutics, membership of the scientific advisory boards of VolitionRx, REPARE Therapeutics and Paige.AI, membership of the Board of Directors of Grupo Oncoclinicas, and ad hoc membership of the scientific advisory boards of Roche Tissue Diagnostics, Ventana Medical Systems, Novartis, Genentech and InVicro. R.R. is founder of GenoTwin and a member of the Scientific Advisory Board of AimedBio in a project unrelated to the current manuscript. S.C. has served as a consultant for Eli Lilly, Novartis, Context Therapeutics, Sermonix, Paige AI, and BMS; S.C. has received prior research funding from Daiichi-Sankyo unrelated to this manuscript.

Abstract

Mutations in the core RNA splicing factor *SF3B1* are prevalent in leukemias and uveal melanoma but hotspot *SF3B1* mutations are also seen in epithelial malignancies such as breast cancer. Although hotspot mutations in *SF3B1* alter hematopoietic differentiation, whether *SF3B1* mutations contribute to epithelial cancer development and progression is unknown. Here, we identify that *SF3B1* mutations in mammary epithelial and breast cancer cells induce a recurrent pattern of aberrant splicing leading to activation of AKT and NF- κ B, enhanced cell migration, and accelerated tumorigenesis. Transcriptomic analysis of human cancer specimens, *MMTV-cre Sf3b1*^{K700E/WT} mice, and isogenic mutant cell lines identified hundreds of aberrant 3' splice sites (3'ss) induced by mutant SF3B1. Consistently between mouse and human tumors, mutant SF3B1 promoted aberrant splicing (dependent on aberrant branchpoints as well as pyrimidines downstream of the cryptic 3'ss) and consequent suppression of PPP2R5A and MAP3K7, critical negative regulators of AKT and NF- κ B. Coordinate activation of NF- κ B and AKT signaling was observed in the knock-in models, leading to accelerated cell migration and tumor development in combination with mutant PIK3CA but also hypersensitizing cells to AKT kinase inhibitors. These data identify hotspot mutations in *SF3B1* as an important contributor to breast tumorigenesis and reveal unique vulnerabilities in cancers harboring them.

INTRODUCTION

Comprehensive genomic analyses of cancer have identified change-of-function mutations in RNA splicing factors to be recurrent across a variety of disparate cancer types (1). Akin to driver oncoproteins, these mutations occur as heterozygous mutations recurrently affecting the same nucleotide positions (so-called “hotspot” mutations). Hotspot mutations occur in both the protein (2-5) as well as RNA components of the spliceosome (6, 7) and globally alter pre-mRNA recognition by the spliceosome in a manner distinct from loss of function (8-10). Malignancies of the hematopoietic system including myeloid neoplasms and chronic lymphocytic leukemia (CLL) harbor a high frequency of these alterations and have been subject to detailed mechanistic investigations into the consequences of mutation on splicing, transcription, and cancer phenotypes (11-15).

SF3B1 is the most commonly mutated RNA splicing factor and studies of hotspot mutations in *SF3B1* have demonstrated that these mutations promote usage of aberrant branchpoint nucleotides (8, 16). Recent functional investigations of aberrant splicing driven by mutant *SF3B1* in the context of myelodysplastic syndromes (MDS), CLL, and uveal melanoma (UVM) have begun to elucidate specific aberrant splicing events required for the maintenance of *SF3B1* mutant cancers (11). In addition, a number of studies in the context of myeloid leukemias have identified that *SF3B1* mutations confer therapeutic vulnerabilities to further modulation of splicing (17) as well as specific metabolic perturbations (18). However, to date, the biological consequences of expression of the same hotspot mutations in *SF3B1* in epithelial-derived malignancies are largely unknown and makes for an intriguing counterpoint. Whilst kinase oncoproteins like BRAF or NTRK function as targetable drivers in different tissue types (19-22), it is unknown whether large-scale modification of RNA splicing in different cell types is similarly oncogenic and utilizes the same pathways within distinct tissues to derive tumor phenotypes.

In this study, we investigated the consequences of *SF3B1* mutations in breast cancer where across a cohort of >5,000 patients, *SF3B1* alterations are observed in ~3% of unselected cases. The effect of mutation upon global splicing, RNA expression, tumorigenesis, and tumor phenotypes highlight how aberrant splicing patterns are conserved but lead to lineage-specific effectors and phenotypes as well as novel therapeutic opportunities. Our data identify that mutations in *SF3B1* promote breast cancer development and progression via aberrant splicing and expression of intermediary signaling proteins that normally negatively regulate AKT and NF- κ B signaling in mammary epithelial cells.

RESULTS

***SF3B1* mutations are enriched in estrogen-receptor positive (ER+) breast cancer and associate with poor outcomes**

To systematically establish the prevalence and significance of *SF3B1* mutations in breast cancer, we performed large-scale analysis of genomic/exomic sequencing data of 5,366 breast cancer patients including prior data from METABRIC, TCGA, and MSK-IMPACT databases (23-25) (**Figure 1A** and **Table S1**). Genetic alterations in *SF3B1*, including mutations, gene fusions, and copy number amplification, were identified in 152 patients (2.83%) (**Figure 1A**), among which 90 patients (1.68%) carried hotspot mutations previously identified as genomic hotspots (26). The K700E ($n=74$) substitution in *SF3B1* was the dominant *SF3B1* mutation in breast cancer patients, followed by hotspot mutations at K666 ($n=5$), N626 ($n=3$), and R625 ($n=2$) residues (**Figure 1B**). Among the patients with hotspot *SF3B1* mutations, ER status was available for 89 patients, only two of which were ER negative (**Figure 1A** and **Table S2**). These two patients both had hormone receptor positive primary cancer and later developed metastatic ER negative tumors. Within the METABRIC and TCGA cohorts where Pam50 and claudin low subtyping is annotated, we found 84% (45/53) of *SF3B1* mutations occurred in luminal A or B subtypes, and 60% (32/53) of the cases were significantly enriched in luminal A breast cancer ($p=0.002$) (**Figure S1**). In terms of other genomic alterations, *SF3B1* hotspot mutations significantly co-occurred with *PIK3CA* mutations ($n=55$ (2.76% in patients with *PIK3CA* mutations), Log_2 odds ratio=1.382, $q<0.001$, **Figure S1**). Interestingly, most *SF3B1* mutant samples that did not carry *PIK3CA* mutations harbored mutations in *PTEN* or *AKT1*, each of which converges on activating PI3K signaling.

Given recent identification that ER positive breast cancers frequently harbor several subclonal mutations that arise under the selection of endocrine targeted therapy (25, 27, 28), we next evaluated the clonality of *SF3B1* mutations in our MSK-IMPACT cohort. Across tumors, mutations in *SF3B1* were clonal with a median allele frequency of ~50%, without manifesting allelic imbalances characteristic of mutant *PIK3CA* (**Figure 1C**). This latter finding is consistent with recent work from our group and others identifying essentiality of the WT allele in cells bearing hotspot change-of-function mutations in *SF3B1* and other RNA splicing factors (29-31). In considering the progression of tumors from primary to metastatic disease, genetic analysis of primary tumors and metastases from a series of *SF3B1* mutant patients identified frequent co-occurrence of *SF3B1* and *PIK3CA* mutations across primary tumors and metastases cases (**Figure 1D**).

We further analyzed the clinical outcomes of patients with *SF3B1* hotspot mutation and *PIK3CA* mutations (**Figure 1E**). The median survival time of ER-positive breast cancer patients with no somatic alteration in either *SF3B1* or *PIK3CA* was 164 months, whereas that of patients with ER-positive

disease harboring both *SF3B1* and *PIK3CA* mutations was 100.1 months (hazard ratio=1.787, $p=0.046$). Neither *SF3B1* nor *PIK3CA* mutation alone was associated with significantly shorter survival. These findings point to *SF3B1* mutation as a recurrent alteration in ER-positive and *PIK3CA* mutant breast cancer that appears to be an early event and linked to poor prognosis.

***Sf3b1*^{K700E} promotes accelerated mammary tumor progression**

To determine the functional role of *SF3B1* hotspot mutations in breast tumorigenesis and progression, we generated a conditional knock-in mouse model to express the most common *SF3B1* mutation found in breast cancer patients (the K700E mutant) from the endogenous *Sf3b1* locus in mouse mammary gland (32). Heterozygous *MMTV-cre Sf3b1*^{K700E/WT} mice expressed mutant *Sf3b1* transcripts in mammary epithelial cells (sorted live, CD45⁻ CD24⁺ cells) at a 50% allelic frequency in RNA (similar to allelic frequency observed in human breast cancers (**Figure 1C**; **Figure S2A-C**)). Due to the significant co-occurrence of *SF3B1* mutation and alterations activating the PI3K pathway, particularly *PIK3CA* mutations in breast cancer patients (**Figure S1**), we further crossed *MMTV-cre Sf3b1*^{K700E/WT} mice with mice bearing a transgenic kinase domain mutation in *PIK3CA* from the *ROSA26* locus (*Rosa26 lox-stop-lox Pik3ca*^{H1047R} (*R26-LSL-Pik3ca*^{H1047R}) (33)) to evaluate the combinatorial effects of these mutations on mammary tumor development and progression.

Whole mount examination of mammary glands from 4-month-old, nulliparous mice of each genotype revealed ductal hyperplasia in mice expressing *Pik3ca*^{H1047R} alone (*MMTV-cre R26-LSL-Pik3ca*^{H1047R}) and in combination with mutant *Sf3b1* (**Figure 2A** and **Figure S2D**). Interestingly, reduced branching of mammary ducts was observed in *MMTV-cre Sf3b1*^{K700E/WT} mice (**Figure S2D**). With further age, *PIK3CA* single-mutant and *Sf3b1*^{K700E/WT}/*Pik3ca*^{H1047R} double mutant mice (*MMTV-cre Sf3b1*^{K700E/WT} *R26-LSL-Pik3ca*^{H1047R}) went on to develop mammary gland tumors (**Figure 2B-C**), while *MMTV-cre Sf3b1*^{K700E/WT} mice did not exhibit any clear pro-tumorigenic phenotype, which is consistent with previous studies with hematopoietic stem cells (14, 30) and B-cells (34, 35) where *Sf3b1* K700E mutation alone was not sufficient to mediate tumorigenesis. Strikingly, the life span of double mutant mice (median=211 days) was significantly shorter than *Pik3ca* single mutant mice (median=293 days, $p=0.0125$, **Figure 2C**). Akin to the tumors *MMTV-cre R26-LSL-Pik3ca*^{H1047R} mice developed, *MMTV-cre Sf3b1*^{K700E/WT} *R26-LSL-Pik3ca*^{H1047R} mice develop lesions within the spectrum of tumors reported in *Pik3ca* conditional mouse models (36), including adenomyoepitheliomas and adenosquamous carcinomas (**Figure S3A**). The adenomyoepitheliomas were composed of a proliferation of gland-like structures lined by a dual cell population of luminal epithelial (CK8/18 and Gata3 staining in **Figure S3A**) and myoepithelial cells (Sma staining in **Figure S3A**), whereas the adenosquamous carcinomas were composed of a complex admixture of gland-like structures, sheets of squamous cells (CK14

staining in **Figure S3A**) and occasional squamous pearls; areas of necrosis were observed. No other histologic abnormalities were detected in the liver, lungs, kidneys, adrenals, spleen, heart, and central nervous system of these mice. Given that *MMTV-cre* has been reported to be expressed in tissues besides mammary epithelial cells (including expression in salivary gland and lymphocytes) (37), we examined both the salivary gland and performed a comprehensive analysis of hematopoietic tissues but did not identify overt malignancies in these tissues at the time of breast tumor formation (**Figure S3B** and **Figure S4**). To characterize the mammary gland tumors that developed in these mice, we probed ER, progesterone receptor (PR), HER2, and Ki67 in representative tumor sections. Whilst all tumors collected were ER positive, PR positive, and HER2 negative, Ki67 staining was significantly higher in tumors from *MMTV-cre Sf3b1^{K700E/WT} Pik3ca^{H1047R}* mice than in those from *Pik3ca^{H1047R}* single mutant mice (**Figure 2D**). We next sought to understand the mechanistic basis by which *SF3B1* mutation could contribute to accelerated progression that was observed both in the mouse and human data.

Pan-cancer and breast cancer-specific aberrant splicing events induced by mutant SF3B1

Prior work in hematopoietic-derived cells and UVM has revealed that cancer-associated mutations in *SF3B1* result in splicing events that utilize aberrant branchpoint nucleotides, manifesting in increased use of aberrant (or so called “cryptic”) intron-proximal 3' splice sites (3'ss) (16, 38). To understand the impact of *SF3B1* mutations on splicing in breast cancers compared to other malignancies, we performed a pan-cancer transcriptomic analysis to identify and quantify cryptic 3'ss usage across *SF3B1* WT versus mutant cancers (**Figure 3**). For breast cancer, RNA-seq data from 20 tumors harboring *SF3B1* mutations and 20 randomly selected, ER-positive WT tumors were collected from the TCGA breast cancer (BRCA) database (**Table S3**). In this analysis, we also included an isogenic pair of parental and *SF3B1* K700E knock-in MCF10A breast epithelial cells, as well as MCF7 and T47D breast cancer cells ectopically expressing *SF3B1* WT, or *SF3B1* K700E mutant via a doxycycline-inducible expression system (**Figure S5**). The expression of the *SF3B1* K700E mutant did not significantly affect cell proliferation and dependence on ER of these breast cancer cells under *in vitro* culture conditions (**Figure S5**). For the comparison of *SF3B1* mutant breast cancer to other cancer types bearing *SF3B1* mutations, RNA-seq data of 15 CLL and 16 UVM patients together with same number of randomly chosen WT samples of the same histologic types of cancer were also included (**Table S3**). Principal component analysis and unsupervised hierarchical clustering of cryptic 3'ss usage using the PSI matrix (**Figure 3A**, **Figure S6** and Methods) robustly separated samples with *SF3B1* hotspot mutations from WT cases with the exception of one breast cancer sample with an *SF3B1* K666N mutation (a result likely explained by the low allelic frequency (7%) of the mutation in the RNA-seq data from this sample).

Samples with non-hotspot *SF3B1* mutations (e.g. S455V, E802Q) clustered together with *SF3B1* WT samples (**Figure S6** and **Table S3**), suggesting that these mutations do not cause aberrant 3'ss usage. Within the *SF3B1* mutant group, samples clustered separately into subgroups by their cancer types. Breast cancer patient and cell line samples (triangles in **Figure 3A**) showed a very similar pattern of aberrant splicing, compared to CLL (circles in **Figure 3A**) or UVM samples (squares in **Figure 3A**), suggesting the aberrant 3'ss usage induced by *SF3B1* mutations in distinct cancers may be due to intrinsic gene expression patterns unique to cell lineage.

Consistent with previous studies in other cancer types (16, 38), most aberrant 3'ss in *SF3B1* mutant breast tumors were located 10 to 30 nucleotides upstream of the canonical 3'ss (**Figure 3B**). For most unaffected 3'ss, a stretch of pyrimidine nucleotides (known as a "polypyrimidine tract") is present within the intron, near the canonical 3'ss. To understand the mechanism by which *SF3B1* mutations affect 3'ss recognition, we analyzed the sequences around cryptic 3'ss promoted in *SF3B1* mutant cells (see Methods; **Figure 3C**). As previously reported, this revealed that polypyrimidine tracts at cryptic 3'ss were interrupted by adenines, indicating a shorter distance between the cryptic 3'ss and branchpoint nucleotides (8, 16). At the same time, we also identified an enrichment of pyrimidines downstream of the aberrant 3'ss. Since most cryptic 3'ss were within 30 nucleotides upstream of the canonical 3'ss, this enrichment could be due to a bias from the polypyrimidine track associated with the canonical 3'ss. To eliminate this bias, we performed a sequence analysis exclusively on cryptic sites 50 nucleotides away from the canonical 3'ss. This analysis continued to reveal significant enrichment of pyrimidines within these 90 aberrant 3'ss ($p < 0.0001$, Fisher's exact test, **Figure 3C**). These data indicate that recognition of cryptic 3'ss by mutant *SF3B1* may require downstream pyrimidine-rich motifs, a finding which was evident across *SF3B1* mutant cancer types.

Aberrant splicing mediated suppression of PPP2R5A and MAP3K7 in *SF3B1*-mutant breast cancers

To identify the key cellular processes that mutant *SF3B1* alters in accelerating breast cancer progression, we performed a gene set enrichment analysis (GSEA) upon the RNAs derived from WT and *SF3B1* mutant breast cancer cell lines. This revealed that inflammatory response pathways (p -value = 0), and NF- κ B signaling (p -value = 0.002) in particular, were significantly altered in *SF3B1* K700E-expressing breast cancer cell lines (**Figure 4A**). Moreover, GSEA analysis on the TCGA BRCA gene expression data also revealed upregulation of these same pathways in the patient samples bearing hotspot *SF3B1* mutations (**Figure S7A**). To verify activation of NF- κ B signaling as a result of mutant *SF3B1* expression, we performed Western blot analysis to assess phosphorylation of p65 (RelA), a core subunit of NF- κ B complex, in isogenic *SF3B1* K700E knock-in MCF10A cells and MCF7

cells expressing mutant SF3B1 (**Figure 4B** and **Figure S7B**). Phosphorylation of p65 was upregulated by 3-5 fold in mutant SF3B1-expressing cells, and the levels of phosphorylation were further enhanced following stimulation by TNF α (**Figure 4B** and **Figure S7B**). To further assess the significance of this activation of NF- κ B, we examined the effect of *SF3B1* mutation on the expression of inflammatory cytokines known to be regulated by NF- κ B. We measured the quantity of secreted cytokines in the culture media of MCF10A and MCF7 WT versus *SF3B1* K700E expressing cells. IL-1a, IL-8, and TGF α were all increased in the media derived from *SF3B1* K700E MCF10A cells (**Figure 4C**), and mutant SF3B1-expressing MCF7 cells produced 10-fold more IL-8 than SF3B1 WT counterpart isogenic cells (**Figure 4C**), consistent with the observed upregulation of p65 phosphorylation in these cells. Upregulated IL-8 secretion in both MCF10A and MCF7 cells expressing mutant SF3B1 was also confirmed by ELISA (**Figure 4D**). These data together confirm the induction of NF- κ B signaling observed in the GSEA analysis of *SF3B1* mutant tumors.

To understand the molecular mechanisms for NF- κ B activation in *SF3B1* mutant cells, we examined the intersection of differentially expressed and differentially mis-spliced genes in human tumors, cell lines, and our mouse model (**Figure 4E** and **Figure S7C**). From this intersection, only two genes were identified: *MAP3K7* and *PPP2R5A*, both of which were significant reduced in expression in *SF3B1* mutants (**Figure 4E** and **Table S4-6**). Of note, these mis-splicing events in *MAP3K7* and *PPP2R5A* have been reported in hematopoietic malignancies with *SF3B1* mutations recently by Lee et al. (30) and Liu et al.(35).

Mutant SF3B1 causes aberrant splicing of *MAP3K7*, stimulating NF- κ B signaling

MAP3K7 has known roles in regulating NF- κ B signaling (39-41) and so we initially sought to verify its mis-splicing and biologic contribution to mutant SF3B1 mediated pathogenesis. To confirm a consistent effect of *SF3B1* mutation on *MAP3K7* splicing and expression, we examined the RNA-seq data of the isogenic cell lines, mouse mammary tissue, and human tumors at the candidate intron where mis-splicing was implicated (**Figure 5A-C**). Across these samples, mutant SF3B1 led to aberrant splicing of *MAP3K7* via use of a cryptic 3'ss that was conserved in human breast cell lines and tumors and mouse mammary gland expressing *Sf3b1*^{K700E} (**Figure 5A-B**). As expected, NMD caused by mis-splicing led to reduced *MAP3K7* transcript and protein levels in mutant SF3B1-expressing cells and mouse mammary gland tumors (**Figure 5C-E** and **Figure S8A**).

To understand this aberrant splicing event in *MAP3K7* in greater molecular detail, we mapped the branchpoints in the aberrantly spliced intron by lariat RT-PCR. Sequencing of the PCR products identified the branchpoints used for the canonical as well as cryptic 3'ss (**Figure S9A**). The branchpoint

for the canonical 3'ss was an adenine 22 nucleotides upstream of the intron-exon boundary, whereas the branchpoint for the cryptic 3'ss mapped to an adenine 14 nucleotides upstream of the aberrant intron-exon boundary (**Figure 5F**). To identify *cis* nucleotides required for mutant SF3B1-specific aberrant splicing of *MAP3K7*, we generated a minigene construct that contains sequences from the mis-spliced intron and flanking exons. As with the endogenous *MAP3K7* transcript, mutant SF3B1 also enhanced usage of a cryptic 3'ss in the minigene-derived *MAP3K7* RNA (**Figure 5F**). Substitution of adenines at the branchpoint with guanines blocked the usage of the cryptic 3'ss (**Figure 5F**). A pyrimidine-rich motif was located in the sequences downstream of the cryptic 3'ss. We mutated thymine nucleotides within this pyrimidine-rich motif to test if these residues were necessary for mutant-SF3B1-specific splicing. Substitution of either two or three thymines to adenines completely abolished the usage of the cryptic 3'ss and aberrant inclusion of the 20-nucleotide intronic sequences (**Figure 5F**). These data identify requirement of the aberrant branchpoint as well as pyrimidines downstream of the aberrant branchpoint in mis-splicing *MAP3K7*.

We next sought to establish the biologic role for MAP3K7 in NF- κ B signaling in breast cancer cells as its regulation of NF- κ B signaling, which has been previously shown to be cell-type specific (39-41). To characterize the impact of MAP3K7 on N-F κ B activation in breast cells specifically, we manipulated MAP3K7 activity in MCF7 and MCF10A cells. Knockdown of MAP3K7 greatly increased phosphorylation of p65 and reduced p38 phosphorylation (**Figure 5G** and **Figure S8B**), which was also observed with pharmacological inhibition of MAP3K7 using 5Z-7-oxozeaenol (42) (**Figure S8C**). Consistent with this, restored expression of MAP3K7 (via expression of MAP3K7 cDNA) in *SF3B1* K700E isogenic MCF10A cells or MCF7 expressing mutant SF3B1 greatly reduced NF- κ B activation and promoted p38 phosphorylation (**Figure 5H** and **Figure S8D**). Taken together, these data establish mutant SF3B1 directed mis-splicing of *MAP3K7* to be a key mediator of enhanced NF- κ B signaling in breast cancer.

Mutant SF3B1 causes aberrant splicing of PPP2R5A, enhancing AKT activation and inflammatory signaling

In addition to mis-splicing of *MAP3K7*, *SF3B1* K700E mutation also induced usage of a cryptic 3'ss 13 nucleotides upstream the normal 3'ss of intron 4 of *PPP2R5A* in human and mouse cells (**Figure 6A-B**). *PPP2R5A* encodes the alpha isoform of the B56 regulatory subunit of PP2A (the serine/threonine-protein phosphatase 2A). PP2A is one of four major serine/threonine phosphatases, and it is a heterotrimeric protein consisting of a catalytic C subunit, one structural A subunit, and a regulatory B subunit. Thirteen distinct genes encoding for the different regulatory B subunits and the specific B subunit expressed regulates substrate selectivity and catalytic activity of PP2A.

Mutant SF3B1 promoted the inclusion of 13 intronic nucleotides in exon 5 by using an upstream cryptic 3'ss, resulting in a reading frame shift (**Figure 6A-B**). This is predicted to cause NMD of the aberrantly spliced *PPP2R5A* transcript and, consistent with this, SF3B1 mutant patient breast tumors had significantly reduced *PPP2R5A* mRNA and protein expression compared to WT (**Figure 6C-D** and **Figure S10A**). As with *MAP3K7*, mis-splicing of *PPP2R5A* by mutant *SF3B1K700E* could be replicated within a *PPP2R5A* minigene and this mis-splicing was abolished by disruption of branchpoint (**Figure 6E** and **Figure S9B**) or interruption of the poly-pyrimidine tract with non-pyrimidines (**Figure 6E**).

PP2A has been reported to regulate phosphorylation of a variety of signaling proteins, including AKT, MEK1/2, and MYC, the downstream consequence of which could be NF- κ B signaling. We therefore probed known PP2A substrates in the context of breast epithelial cells by Western blot and found increased phosphorylation of AKT at residue T308 in breast cells expressing mutant SF3B1 (**Figure 6D** and **Figure S10A**). Knockdown of *PPP2R5A* in MCF10A and MCF7 cells by shRNA also upregulated phosphorylation of p65 and AKT (at T308) (**Figure 6F** and **Figure S10B**). Furthermore, depletion of *PPP2R5A* in cells also induced expression of inflammatory response genes, including IL-8, CDKN1A, IL-1A, and CXCL1 (**Figure 6G**). Restoration of *PPP2R5A* expression in MCF7 cells expressing mutant SF3B1 or isogenic *SF3B1^{K700E/WT}* MCF10A cells showed consistently reduced phosphorylation of p65 and AKT (**Figure S10C**). Given the known roles of AKT in regulating IKK and NF- κ B activation, our data point to *PPP2R5A* downregulation as a second mechanism whereby mutant SF3B1 promotes NF- κ B signaling in breast cancer.

***SF3B1* mutations promote invasion and migration of breast cancer cells**

NF- κ B signaling has been implicated in regulating cell migration of breast cancer cells (43-45). To test if *SF3B1* mutation facilitates cell migration, we initially performed wound-healing assays. MCF7 cells expressing mutant SF3B1 traversed wounds significantly faster than the cells expressing WT SF3B1 or empty vector (**Figure 7A**) irrespective of stimulation by TNF α . Comparable differences were also seen with MCF10A isogenic pairs (**Figure 7B**).

Since *SF3B1* mutant cells secrete more inflammatory cytokines (including IL-8), we hypothesized that the higher migration might be mediated by cytokines within the culture media. To address this possibility, we harvested media from cells expressing WT or mutant SF3B1 and studied the effect of media addition upon migration of parental MCF7 cells in wound-healing assays. WT MCF7 cells exposed to media from mutant SF3B1-expressing cells healed wounds faster than controls (**Figure 7C**). In addition to cellular motility, NF- κ B signaling has been linked to breast cancer invasiveness and we thus investigated the effects of *SF3B1* mutation in transwell Matrigel invasion

assays. MCF10A breast epithelial cells hardly invaded Matrigel, whereas significantly more *SF3B1* K700E knock-in MCF10A cells migrated through the Matrigel layer (**Figure 7D**). Moreover, we assess for enhanced invasiveness using a xenograft assay (**Figure 7E**) in which limiting quantities of WT and mutant *SF3B1* expressing MCF7 cells were implanted into NSG mice and observed the *SF3B1* mutant tumors grew to significantly larger size despite equivalent growth rates for the corresponding cell line models in 2D culture conditions.

As mis-splicing of *MAP3K7* and *PPP2R5A* induced by mutant *SF3B1* mediates dysregulation of NF- κ B, we further tested the role of these proteins on cell migration. Knockdown of either *MAP3K7* or *PPP2R5A* enhanced cell migration (**Figure S11A-B** and **S12A-B**), and restoring these proteins in *SF3B1* mutant cells restrain cell migration as assessed in wound-healing assays (**Figure S11C-D** and **S12C-D**). These data indicate that mutant *SF3B1* mediated dysregulation of NF- κ B signaling enhances breast cancer migration and invasion.

***SF3B1*K700E mutations sensitize breast cancer cells to AKT inhibitors**

While the independent splicing events identified above converge upon promoting NF- κ B signaling and associated phenotypes, therapeutic approaches targeting NF- κ B have proven challenging. By contrast, PI3K/AKT inhibition has shown some efficacy in breast cancer and so we sought to determine whether suppression of *PPP2R5A* might increase tumor dependence on AKT for growth and viability. Given the induction of AKT T308 phosphorylation in *SF3B1* K700E knockin cells we evaluated the effects of *SF3B1* mutation upon a set of established downstream substrates of activated AKT in breast cancer cells. In isogenic MCF7 breast cancer cells, expression of *SF3B1* K700E increased phosphorylation of FOXO1, PRAS40 and ribosomal protein S6 (**Figure 8A** and **Figure S13A**), further confirming AKT activation. Recent studies have suggested that increased signaling output through PI3K/AKT can enforce heightened dependence and drug sensitivity. We therefore evaluated the effect of expression of mutant *SF3B1*^{K700E} on selective inhibitors of AKT. We examined the effect of both an allosteric pan-AKT inhibitor, MK2206, as well as an ATP-competitive pan-AKT inhibitor GDC0068 in MCF7 cells, which are *PIK3CA* mutant and sensitive to AKT inhibitors, and observed a 2.5-4x further reduction in the IC₅₀ as a result of *SF3B1* mutation (**Figure 8B**). Finally, to examine the sensitivity of MCF10A cells to AKT inhibitors, we created MCF10A cells with heterozygous knockin of *PIK3CA*^{H1047R} in the endogenous locus of *PIK3CA* with or without combined *SF3B1*^{K700E/WT} knockin (**Figure S13B**). These cells exhibited comparable splicing alterations of *MAP3K7* and *PPP2R5A*, as well as activation of NF- κ B signaling (**Figure S14A**). Mutant *PIK3CA*^{H1047R} induced expression of inflammatory response genes and promoted cell migration, which was further enhanced in the cells with both *SF3B1*^{K700E} and *PIK3CA*^{H1047R} mutations (**Figure S14**). Knockin of *PIK3CA*^{H1047R} relieved the dependency of MCF10A

cells on epidermal growth factor (EGF) supplemented to culture media and activated PI3K-AKT signaling pathway (**Figure 8C** and **Figure S13C**). Again, in these cells, expression of mutant SF3B1 enhanced the sensitivity of *PIK3CA* mutant cells to inhibition of AKT (**Figure 8D**). This enhanced sensitivity of *PIK3CA* mutant cells induced by *SF3B1* mutation was also confirmed by clonogenic survival assays (**Figure 8E-F**), in which 2.5-5x reduction in IC₅₀ was associated with expression of the *SF3B1* mutation. Together, these data suggest that *SF3B1* mutant tumors as a unique subset of breast cancers wherein coordinate mutational activation of signaling together with suppression of a key negative regulator PPP2R5A leads to enhanced sensitivity of AKT inhibitors that are under current investigation in the clinic.

DISCUSSION

Identifying and targeting oncogenic pathways stimulated by gain-of-function genomic alterations has resulted in major clinical advances in outcomes for breast cancer patients (46-50). The recent comprehensive genomic analyses of thousands of breast cancer patients has identified a number of subgroups of patients with recurrent genomic alterations ranging from 1-10% and for which deeper understanding of their contribution to tumor growth is lacking (23, 51, 52). As a result, functional investigation of the genetic alterations enriched in these specific subsets of breast cancer patients has become paramount. Successful examples include the use of PD1 blockade in mismatch repair deficient tumors (53), PARP inhibitors in germline *BRCA1/2*-mutant breast cancer (54), or anti-androgen therapy in androgen-receptor-positive triple-negative breast cancer (55, 56). In this work, we identify a novel class of recurrent genetic alterations that appear to promote breast tumorigenesis through modifying the function of the core RNA splicing factor SF3B1. Our data reveal *SF3B1* mutant breast cancers to be a unique transcriptomic subtype of ER+ breast cancers with strong co-enrichment with PI3K/AKT alterations, augmenting AKT and NF- κ B signaling.

Given prior work identifying how *SF3B1* mutations alter splice site sequence preference with attendant effects of select genes (30, 38, 57), we sought to profile aberrant splicing across breast cancers and compare these results with other cancers where *SF3B1* mutations are found. Although the results demonstrated aberrant 3'ss usage shared across *SF3B1* mutant tumors, only a handful of events were shared between different breast cancer samples, isogenic ER+ and ER- breast cancer cell lines, and our mouse breast cancer models. Specifically, our consensus overlap identified only two transcripts shared between cell lines and tumors with convergent alterations in 3' splice site usage and mRNA downregulation- *PPP2R5A* and *MAP3K7*. Importantly, these two events are also observed in other cancer types such as MDS and CLL which identifies them as potentially critical mediators of the effects of mutant SF3B1 across diverse cancer lineages. For both of these mRNAs, mutant SF3B1 promoted usage of an aberrant branchpoint adenosine nucleotide that was required for mis-splicing and the presence of a polypyrimidine tract downstream of the aberrant branchpoint was also necessary for mutant SF3B1 mis-splicing.

Our data demonstrate that *SF3B1* mutation can downregulate expression of both *PPP2R5A* and *MAP3K7* simultaneously and thereby promote AKT and NF- κ B signaling output with resulting increases in breast cancer migration/invasion. Akin to *SF3B1* mutation in hematopoietic stem cells (14, 30) as well as B-cells (34, 35), *SF3B1* mutation alone does not appear sufficient to mediate tumorigenesis in the mammary gland. However, when mutations in *SF3B1* and *PIK3CA* were paired, there was major acceleration in tumor phenotypes observed with the double mutants significantly accelerating tumor formation and lethality. Coinciding with this observation from the mice was the finding that patients with

mutations in both *SF3B1* and *PIK3CA* had an inferior prognosis compared to WT patients.

We speculate that addition of the *SF3B1* mutation to a *PIK3CA* mutant model can serve to reinforce signals initially elicited by PI3K activation. It is well established that PI3K activation promotes feedback suppression of the pathway through a variety of mechanisms such as suppression of RTK signaling (58) as well as inhibition of parallel pathways such as the NF- κ B pathway. Given the widespread mechanisms of feedback suppression of signaling as a result of oncogenic PI3K signaling, there may be stronger selection for genomic alterations that coordinately remodel multiple signaling pathways akin to changes in the epigenome or transcription factors.

Finally, our functional interrogation of the mis-spliced events in *SF3B1* mutant breast cancers nominated specific pathways for therapy of these tumors that might not emerge as obvious from the genotypes alone. We noted that the hyperactivation of AKT signaling that was induced as a result of combined *PIK3CA* and *SF3B1* mutation might engender further therapeutic significance. Recent work has demonstrated that multiple mutations in *PIK3CA* can lead to increases in AKT output that ultimately increases the sensitivity of these tumors to PI3K/AKT inhibition (59). The alteration in PPP2R5A results in changes that serve to further activate AKT signaling and, in like manner, appeared to increase the sensitivity of these tumors to AKT kinase inhibitors. AKT inhibitors are currently under study in ER-positive breast cancers harboring AKT E17K mutations and our data suggest that *SF3B1* mutation could provide an additional patient subset that may be sensitized to these therapies.

METHODS

Human subjects

A total of 1,918 breast tumor specimens from 1,756 patients with breast cancer who underwent prospective clinical genomic profiling were included for study. The demographic and clinical characteristics of the cohort are presented in **Table S2**.

Mutation oncoprint analysis

The mutual mutational pattern of *SF3B1*, *PIK3CA*, *PTEN*, *AKT1*, *TP53*, *MAP3K1*, *ESR1*, *NF1*, *PIK3R1*, *BRCA1*, *ERBB3* and *MYC* was investigated on three breast cancer cohorts including METABRIC, MSK-IMPACT and TCGA (**Figure 1A** and **Figure S1**). The analysis was performed using the online tool from cBioportal website (<https://www.cbioportal.org/oncoprinter>). The raw input files were provided in **Table S1**.

Mutation and allele frequency analysis

We compared the allele frequency of *SF3B1* and *PIK3CA* mutations in $n = 23$ double mutated samples from MSK-IMPACT breast cancer cohort. Variant allele frequency (VAF) was corrected by tumor purity estimated by Immunohistochemistry. Wilcoxon rank sum test was applied to give statistics between the VAF of two mutations.

We analyzed the frequency of somatic mutations in MSK-IMPACT patients ($n = 41$) harboring *SF3B1* hotspot mutations. Mutation frequency was calculated for each reported gene in $n = 25$ primary samples and $n = 20$ metastasis samples respectively.

Animals

All mice were housed at Memorial Sloan Kettering Cancer Center. Generation and genotyping of the *Sf3b1*^{K700E/WT} and *R26-LSL-Pik3ca*^{H1047R} as well as the *MMTV*-cre transgenic mice have been previously described (14, 33). The mice were monitored closely for signs of disease or morbidity daily and were killed when they showed a volume of the visible tumor formation above 1 cm³, failed to thrive, experienced weight loss >10% total body weight or showed open skin lesions, bleeding or any signs of infection.

Whole mount staining of mouse mammary gland

The fourth pair of mammary glands were excised from 4-month-old female mice and stained as described previously (60). Briefly, mammary glands were placed flattened on glass slides and fixed with Carnoy's fixative (ethanol:chloroform:acetic acid, 6:3:1) at room temperature for 4 hours. Then the

glands were gradually rehydrated with 70%, 35%, 17.5% and distilled water. The mammary glands were stained in carmine alum solution (0.2% carmine natural red (Sigma), 0.5% aluminum potassium sulfate (Sigma) in water) overnight at room temperature, and then dehydrated progressively in 70%, 95%, 100% ethanol. The mammary fat pads were then cleared in xylene overnight. The slides were mounted with Permount (Fisher Scientific) and scanned by Panoramic Scanner (3DHISTECH). The mammary epithelial area (MEA) and the numbers of branching points (center) were analyzed using FIJI software as previously described (61). The numbers of terminal buds were counted manually in 10 random 2mm×2mm squares on each slide with QuPath software (62) and presented as number of terminal bud per mm².

Immunohistochemistry

Mouse tissue was collected and fixed in 10% neutral buffered formalin for 48 h. Samples were then processed, embedded in paraffin, sectioned at 4 μm thickness, and stained with hematoxylin and eosin by Laboratory of Comparative Pathology at MSKCC. Immunohistochemical staining was performed on a Ventana Stains System with primary antibodies (listed in **Table S7**) and OmniMap DAB anti-Rb Detection Kit or OmniMap DAB anti-Ms Detection Kit (Ventana). The slides were scanned by Panoramic Scanner (3DHISTECH) and positively stained cell number was counted with QuPath software(62).

Cell lines

Cell lines were maintained in 37°C incubator with 5% CO₂ in humidified atmosphere. MCF7 and MCF10A cells were obtained from ATCC. HEK293T cells were cultured in DMEM with 10% FBS (Gibco). MCF7 cells were grown in DMEM/F12 supplemented with 10% FBS (Gibco), 100 μg/mL penicillin, 100 mg/mL streptomycin (Corning), and 4 mM glutamine, and MCF10A cells were grown in DMEM/F12 supplemented with 5% horse serum (Gibco), 20ng/mL EGF (Sigma-Aldrich), 10μg/mL insulin (Sigma-Aldrich), 0.5μg/mL hydrocortisone (Sigma-Aldrich), 0.1μg/mL cholera toxin (Sigma-Aldrich), 100 μg/mL penicillin, and 100 mg/mL streptomycin (Corning). T47D cells were cultured in RPMI1640 with 10% FBS (Gibco), 100 μg/mL penicillin and 100 mg/mL streptomycin (Corning). For cell proliferation assay, 1000 cells were seeded in each well of 96-well plates, and proliferation was measured with resazurin reagent (Fisher Scientific).

MCF10A *SF3B1*^{K700E/WT} knockin cell lines were generated by Horizon Discovery. MCF10A *PIK3CA*^{H1047R} single and *PIK3CA*^{H1047R} *SF3B1*^{K700E/WT} double knockin cells were generated by CRISPR and homology-directed repair (HDR) as described previously (11). Briefly, guide RNA sequence was cloned into px458-GFP vector (Addgene 48138) and nucleofected into MCF10A WT or *SF3B1*^{K700E/WT}

cells together with a single-stranded donor oligonucleotides (ssODN) as template for HDR using the Lonza Nucleofector V kit and program T-024 on the nucleofector device. The ssODN sequence was CGAAAGACCCTAGCCTTAGATAAAACTGAGCAAGAGGCTTTGGAGTATTTTCATGAAACAAATGAAC GACGCGCGTCACGGTGGCTGGACAACAAAATGGATTGGATCTTCCACACAATTAACAGCATGC ATTGAACTGA. Silent mutations were introduced besides H1047R to avoid Cas9 recognition on the knockin allele. GFP-positive nucleofected cells were single-cell sorted 48 hours after nucleofection. Clones were screen for knockin of *PIK3CA*^{H1047R} by PCR with primers GTTTCAGGAGATGTGTTACAAG and GTGTGGAATCCAGAGTGAGC and subsequent Sanger sequencing.

Plasmids

The SF3B1 expressing lentiviral vector were generated by cloning cDNA of wild-type SF3B1 or SF3B1 K700E with flag tagged at N-terminal end into pInducer20 (Addgene 44012). Lentivirus was prepared in HEK293T cells with pInducer20 empty vector or the plasmid with SF3B1 (wild-type or mutant) cDNA, and then used to transduce breast cell lines. Transduced cells were selected in medium supplemented with 1mg/mL Geneticin (Invivogen) for 2 weeks before being used in the experiments.

shRNAs against PPP2R5A or renilla luciferase were cloned into MLS-E-GFP vector, and the shRNA sequences were: PPP2R5A-1: TTAGTTGAAACATACTCAACCA; PPP2R5A-2: TTTAATTATATTATACTGATGA; Renilla: CAGGAATTATAATGCTTATCTA. Retrovirus was prepared in HEK293T cells and then used to transduce MCF7 or MCF10A cells. GFP positive cells stably expressing shRNAs were selected by FACS 3 days after transduction.

shRNAs against MAP3K7 or renilla luciferase were cloned into LT3GEPIR vector, and the shRNA sequences were: MAP3K7-1: TTAGGTAAATTTTTTATCAGTG; MAP3K7-2: TTTTCAACAATTTTGATTCTAA. Lentivirus was prepared in HEK293T cells and then used to transduce MCF7 and MCF10A cells. Transduced cells were selected in medium supplemented with 1µg/mL puromycin (Thermo Fisher Scientific) for one week before being used in the experiments. The MAP3K7 and PPP2R5A expression vector was generated by cloning *MAP3K7* or *PPP2R5A* cDNA into pMSCV-GFP retroviral vector to express MAP3K7 or PPP2R5A protein. Retrovirus was prepared in HEK293T cells and then used to transduce MCF7 or MCF10A cells. GFP positive cells stably expressing MAP3K7 or PPP2R5A were selected by FACS 3 days after transduction.

Antibodies

Antibodies used are listed in **Table S7**.

Western blotting

Protein samples were extracted from cultured cells with RIPA buffer (Thermo Scientific) and quantified by BCA assay. Protein fractionated on NuPAGE 4-12% Bis-Tris gels (Life Technologies) was transferred onto nitrocellulose membranes. All primary antibodies (listed in **Table S7**) were used with 1:1000 dilution, except for GAPDH antibody, which was used at 1:5000 dilution in TBST containing 5% BSA and 0.02% sodium azide. Peroxidase conjugated goat anti-rabbit IgG secondary antibody (Sigma-Aldrich) was used at 1:10000 dilution in TBST containing 2.5% skim milk. The blot was then visualized by chemiluminescence. Developed films were scanned and quantitated with FIJI software.

RT-PCR and quantitative RT-PCR

Total RNA was extracted with Qiagen RNeasy mini kit, and cDNA was generated with qScript cDNA SuperMix (Quantabio) according to the manufacturers' instructions. For RT-PCR, the amplification was performed with DreamTaq Hot Start Green PCT Master Mix (Thermo Fisher Scientific) and specific primers. PCR products were fractionated on 10% TBE gel (Life Technologies) and visualized with ethidium bromide. For quantitative RT-PCR, 0.5 μ l cDNA was added to 10 μ l PCR reactions prepared with Taqman Universal PCR Master Mix (Thermo Fisher Scientific) and gene specific Taqman probes. All quantitative RT-PCR analysis was performed on an Applied Biosystems ViiA 7 Real-Time PCR System. Relative gene expression levels were calculated using the comparative CT method. Primers and Taqman probes used in this study are listed in **Table S8**.

Cell migration assay

About 1×10^5 cells were seeded into each well of 12-well plates and cultured until 100% confluence. The "scratch" was created with a p200 pipet tip on the cell monolayer through the center of the well. The debris was removed by washing the well with 1 ml of culture medium and then 1 ml of medium (with 2% serum) specific for the cell migration assay was added into each well. The plate was incubated at 37°C, and images of the "scratch" were captured at various time points with a Zeiss Axiovert Microscope. The width of scratch was measured with FIJI software.

Cell invasion assay

MCF10A cells were cultured to about 70% confluence and serum starved overnight. Harvested by trypsinization, 5×10^4 cells resuspended in serum-free medium (without EGF) were seeded to the Matrigel invasion chamber (8 μ m pore size, Corning) in 24-well plate. Complete culture medium for MCF10A was added to the bottom chambers of each well. After 24-hour incubation, the cells at the bottom side of the chamber were fixed and stained with hematoxylin. The membrane was then cut off

from the chamber and the number of migrating cells were quantified by counting cells under microscope.

Cytokine multiplex assay

Forty-one cytokines and chemokines were analyzed simultaneously with bead-based multiplex assay using Milliplex Map Human Cytokine/Chemokine Magnetic Bead Panel (HCYTMAG-60K-PX41, Millipore) on Luminex FLEXMAP 3D instrument according to the manufacturer's instruction. Briefly, cells were seeded in T25 flask and media were refreshed when the cells approached 70% confluence. Cell culture supernatant was harvested 48 hours after media change and multiplex cytokine assay was performed on Luminex FlexMap 3D instrument. The results were normalized to cell numbers in each flask.

IL-8 ELISA

IL-8 concentration in the culture supernatant was quantified by human IL-8 ELISA kit (RayBiotech) according to the manufacturer's instruction. Briefly, cells were seeded in T25 flask and culture medium was changed when the cells approached 70% confluence. Cell culture supernatant was harvested 48 hours after media change and IL-8 ELISA was performed on SpectraMax M5 microplate reader (Molecular Devices). The results were normalized to cells number in each flask.

Cell Proliferation

Cell proliferation was measured as described previously (63). Briefly, cells (1000/well) were seeded into 96-well plates and treated with different concentrations of indicated drugs. Media and drug were changed every week. On Day 0, 3, 5 and 7, 25 μ l of Resazurin (R&D Systems, Minneapolis, MN, USA) was added to each well and incubated for 4 hours. Fluorescence in the plate was measured using a SpectraMax M5 microplate reader (Molecular Devices). Cell growth data from Day 5 was then plotted as percentage inhibition against the log concentration of indicated drugs. IC_{50} was determined using a sigmoidal regression model using GraphPad Prism 7.0.

Minigene assay

The *PPP2R5A* minigene construct was generated by inserting the DNA fragment containing the *PPP2R5A* genomic sequence from exon 4 to exon 5 in between the KpnI and XhoI restriction sites of pcDNA3.1 vector. The *MAP3K7* minigene construct was generated by inserting the DNA fragment containing the *MAP3K7* genomic sequence from exon 4 to exon 5 at HindIII restriction site of pcDNA3.1 vector. The sequences of the inserted fragments were verified by sanger sequencing. Mutagenesis of minigene constructs was performed with the Agilent QuikChange II site-directed mutagenesis kit with

specific primers according to the manufacturer's directions. For transient transfection experiments, cells were seeded into a 24-well plate with culture medium containing doxycycline 48 hours before transfection of minigene constructs in the presence of X-tremeGENE HP DNA transfection reagent (Roche) according to the manufacturer's directions. Forty-eight hours after transfection, cells were collected, and RNA was extracted using Qiagen RNeasy mini kit. Minigene-derived and endogenous *MAP3K7* and *PPP2R5A* transcripts were analyzed by RT-PCR using specific primers (**Table S8**).

Clonogenic survival assay

Clonogenic survival assay was performed on 6-well plate. 500 hundred cells in single cell suspension were seeded into each well of 6-well plate and treated with various doses of MK2206 on the next day, following which the plate was incubated in 37°C incubator with 5% CO₂ in humidified atmosphere for 14 days (for MCF10A cells) or 21 days (for MCF7 cells). After incubation, the colonies were fixed with formalin and stained with 0.01% crystal violet. The plate was then photographed and analyzed with Oxford GelCount colony counter.

Xenograft assay

NOD scid gamma (NSG) female mice at age of 6-8 weeks were obtained from Jackson Laboratory and maintained in pressurized ventilated caging. This study was performed in compliance with institutional guidelines under an IACUC approved protocol (MSKCC#12-10-016). MCF7 xenograft tumors expressing wild-type or mutant SF3B1 were established in NSG mice by subcutaneously implanting 0.72 mg sustained release 17β-estradiol pellets with a 10g trocar into one flank followed by injecting 1×10⁶ cells suspended 1:1 (volume) with reconstituted basement membrane (Matrigel, Collaborative Research) on the opposite side 3 days afterwards. On the same day of cell inoculation, the mice were fed with filter water containing 2mg/ml doxycycline and 2% sucrose, which was refreshed twice a week. Tumor dimensions were measured with vernier calipers starting from 14 days after cell implantation and tumor volumes were calculated as ($\pi/6 \times \text{larger diameter} \times (\text{smaller diameter})^2$). The experiment was closed 7 weeks after implantation. Based upon our previous work measuring the variability in size and growth of MCF7 xenografts, we estimated 10 mice/group would allow us to detect tumor size differences of >200 mm³.

RNA-seq of breast cancer cell lines and mouse tissues

Total RNA was extracted with Direct-Zol RNA miniprep kit (Zymo). RNA-seq libraries were prepared and sequenced by Genewiz with 150-bp pair-end reads with 100 million read depth.

Heatmap and hierarchical clustering

To explore potential tumor/hotspot specificity or similarity of 3'ss alteration, principal component analysis and unsupervised hierarchical clustering were performed using 618 significantly (q -value < 0.001) differential splicing junctions between all *SF3B1* mutant and all WT samples (See supplemental methods for novel cryptic 3'ss identification). Command 'prcomp' from R package 'stats' was used for the principal component analysis. Command 'heatmap.2' from R package 'gplots' was adopted for the clustering analysis using $1-(\text{Pearson correlation})/2$ as distance. This analysis was performed on TCGA BRCA, MSK breast cancer cell lines (MCF7, T47D and MCF10A), ICGC CLL, dbGaP CLL and TCGA UVM samples.

Sequence motif analysis

We performed motif analysis at aberrant 3'ss as well as the associated canonical 3'ss. We first identified sets of cryptic 3'ss significantly differentially used between *SF3B1* mutant and WT samples by combing TCGA breast cancer samples and MSK cell lines data. Next, motif logo was plot based on the intron nucleotide composition up to 50 nt upstream and 20 nt downstream from the AG dinucleotide of cryptic 3'ss as well as the associated canonical 3' AG site, using R package 'motifStack'. Fisher's exact test was performed to compare the enrichment of pyrimidines in the 10 nt downstream from the AG of cryptic 3'ss to the associated canonical 3' AG site.

GSEA analysis

We used GSEA software (64) with defined hallmark genesets (MSigDB, v6.1) to investigate molecular profiles enriched in *SF3B1* mutant breast cancer samples. Parameters used were, Collapse data: false, Permutation type: gene set, 1000 permutations, Chip platform: gene symbol. The input gene expression matrix contains 10165 genes, which are significantly differentially expressed (DE) between *SF3B1* mutations and WT on cell line data (combing the DE lists from MCF7, T47D, and MCF10A).

Expression dataset and differential expression

To generate mRNA expression matrix for transcriptome analysis, we used featureCounts (65) from package 'Subread' to call read counts from STAR re-aligned bam files. Genes with low read depths across the cohort are removed. Then, read counts are transformed into RPKM values, followed by \log_2 transformation, and quantile normalized on sample level. We also performed DESeq2 analysis (66) (using the raw read counts) to call differential expressed genes between *SF3B1* mutant and WT TCGA breast cancer samples and MSK cell lines data.

Data availability

The RNA sequencing data have been deposited in NCBI Sequence Read Archive (SRA) under accession number GSE145471.

Statistics

Statistical significance was determined by (i) unpaired or paired two-sided Student's t-test after testing for normal distribution, (ii) one-way or two-way ANOVA followed by Dunnett's, Tukey's multiple comparisons tests, or (iii) Kruskal-Wallis tests with Dunn's test corrected for multiple comparisons. Data were plotted using GraphPad Prism 7 software as individual points with mean values and error bars representing standard deviation.

Study approval

This study was approved by the Memorial Sloan Kettering Cancer Center Institutional Review Board (IRB) and all patients provided written informed consent for tumor sequencing and review of patient medical records for detailed demographic, pathologic, and treatment information (NCT01775072). All mouse procedures and experiments were completed in accordance with the Guidelines for the Care and Use of Laboratory Animals and were approved by the Institutional Animal Care and Use Committees at MSKCC (MSKCC#12-10-016).

ACKNOWLEDGMENTS

O.A.-W. and S.C. are supported by the Dept. of Defense Breast Cancer Research Program (W81XWH-18-1-0383), the Functional Genomics Initiative of Memorial Sloan Kettering Cancer Center, and the NCI Cancer Center Support Grant (CCSG, P30 CA08748). S.C. also acknowledges support by the Breast Cancer Research Foundation for this work.

AUTHOR CONTRIBUTIONS

B.L. Z.L., R.R., O.A.-W., and S.C. designed the study. B.L., S.C., M.K., C.E., Q.C., and E.d.S. performed the animal experiments. B.H.D. and J.S.R.-F. assisted with pathological analysis. B.L., Z.L., Y.S., and R.R. performed RNA-seq analyses. B.L. O.A.-W., and S.C. performed *in vitro* cell line experiments. B.L., Z.L., O.A.-W., and S.C. wrote the manuscript.

REFERENCES

1. Seiler M, Peng S, Agrawal AA, Palacino J, Teng T, Zhu P, et al. Somatic Mutational Landscape of Splicing Factor Genes and Their Functional Consequences across 33 Cancer Types. *Cell reports*. 2018;23(1):282-96 e4.
2. Yoshida K, Sanada M, Shiraishi Y, Nowak D, Nagata Y, Yamamoto R, et al. Frequent pathway mutations of splicing machinery in myelodysplasia. *Nature*. 2011;478(7367):64-9.
3. Wang L, Lawrence M, Wan Y, Stojanov P, Sougnez C, Stevenson K, et al. SF3B1 and other novel cancer genes in chronic lymphocytic leukemia. *The New England journal of medicine*. 2011;365(26):2497-506.
4. Papaemmanuil E, Cazzola M, Boultonwood J, Malcovati L, Vyas P, Bowen D, et al. Somatic SF3B1 mutation in myelodysplasia with ring sideroblasts. *N Engl J Med*. 2011;365(15):1384-95.
5. Graubert TA, Shen D, Ding L, Okeyo-Owuor T, Lunn CL, Shao J, et al. Recurrent mutations in the U2AF1 splicing factor in myelodysplastic syndromes. *Nat Genet*. 2012;44(1):53-7.
6. Suzuki H, Kumar SA, Shuai S, Diaz-Navarro A, Gutierrez-Fernandez A, De Antonellis P, et al. Recurrent noncoding U1 snRNA mutations drive cryptic splicing in SHH medulloblastoma. *Nature*. 2019;574(7780):707-11.
7. Shuai S, Suzuki H, Diaz-Navarro A, Nadeu F, Kumar SA, Gutierrez-Fernandez A, et al. The U1 spliceosomal RNA is recurrently mutated in multiple cancers. *Nature*. 2019.
8. Darman RB, et al. . Cancer-Associated SF3B1 Hotspot Mutations Induce Cryptic 3' Splice Site Selection through Use of a Different Branch Point. *Cell reports*. 2015;13(5):1033-45.
9. Kim E, Ilagan JO, Liang Y, Daubner GM, Lee SC, Ramakrishnan A, et al. SRSF2 Mutations Contribute to Myelodysplasia by Mutant-Specific Effects on Exon Recognition. *Cancer cell*. 2015;27(5):617-30.
10. Ilagan J, Ramakrishnan, A, Hayes, B, Murphy, ME, Zebari, AS, Bradley, P, Bradley, RK. . U2AF1 mutations alter splice site recognition in hematological malignancies. . *Genome Research (In press)*. 2014.
11. Inoue D, Chew GL, Liu B, Michel BC, Pangallo J, D'Avino AR, et al. Spliceosomal disruption of the non-canonical BAF complex in cancer. *Nature*. 2019;574(7778):432-6.
12. Yoshimi A, Lin KT, Wiseman DH, Rahman MA, Pastore A, Wang B, et al. Coordinated alterations in RNA splicing and epigenetic regulation drive leukaemogenesis. *Nature*. 2019.
13. Ilagan JO, Ramakrishnan A, Hayes B, Murphy ME, Zebari AS, Bradley P, et al. U2AF1 mutations alter splice site recognition in hematological malignancies. *Genome research*. 2014.
14. Obeng EA, Chappell RJ, Seiler M, Chen MC, Campagna DR, Schmidt PJ, et al. Physiologic Expression of Sf3b1(K700E) Causes Impaired Erythropoiesis, Aberrant Splicing, and Sensitivity to Therapeutic Spliceosome Modulation. *Cancer cell*. 2016;30(3):404-17.
15. Wang L, Brooks AN, Fan J, Wan Y, Gambe R, Li S, et al. Transcriptomic Characterization of SF3B1 Mutation Reveals Its Pleiotropic Effects in Chronic Lymphocytic Leukemia. *Cancer cell*. 2016;30(5):750-63.
16. DeBoever C, Ghia EM, Shepard PJ, Rassenti L, Barrett CL, Jepsen K, et al. Transcriptome sequencing reveals potential mechanism of cryptic 3' splice site selection in SF3B1-mutated cancers. *PLoS computational biology*. 2015;11(3):e1004105.
17. Seiler M, Yoshimi A, Darman R, Chan B, Keaney G, Thomas M, et al. H3B-8800, an orally available small-molecule splicing modulator, induces lethality in spliceosome-mutant cancers. *Nature medicine*. 2018.
18. Dalton WB, Helmenstine E, Walsh N, Gondek LP, Kelkar DS, Read A, et al. Hotspot SF3B1 mutations induce metabolic reprogramming and vulnerability to serine deprivation. *J Clin Invest*. 2019;130:4708-23.
19. Drilon A, Laetsch TW, Kummar S, DuBois SG, Lassen UN, Demetri GD, et al. Efficacy of Larotrectinib in TRK Fusion-Positive Cancers in Adults and Children. *N Engl J Med*. 2018;378(8):731-9.

20. Pratilas CA, Taylor BS, Ye Q, Viale A, Sander C, Solit DB, et al. (V600E)BRAF is associated with disabled feedback inhibition of RAF-MEK signaling and elevated transcriptional output of the pathway. *Proc Natl Acad Sci U S A*. 2009;106(11):4519-24.
21. Hyman DM, Puzanov I, Subbiah V, Faris JE, Chau I, Blay JY, et al. Vemurafenib in Multiple Nonmelanoma Cancers with BRAF V600 Mutations. *The New England journal of medicine*. 2015;373(8):726-36.
22. Diamond EL, Durham BH, Ulaner GA, Drill E, Buthorn J, Ki M, et al. Efficacy of MEK inhibition in patients with histiocytic neoplasms. *Nature*. 2019;567(7749):521-4.
23. Cancer Genome Atlas N. Comprehensive molecular portraits of human breast tumours. *Nature*. 2012;490(7418):61-70.
24. Curtis C, Shah SP, Chin SF, Turashvili G, Rueda OM, Dunning MJ, et al. The genomic and transcriptomic architecture of 2,000 breast tumours reveals novel subgroups. *Nature*. 2012;486(7403):346-52.
25. Razavi P, Chang MT, Xu G, Bandlamudi C, Ross DS, Vasan N, et al. The Genomic Landscape of Endocrine-Resistant Advanced Breast Cancers. *Cancer Cell*. 2018;34(3):427-38 e6.
26. Chang MT, Bhattarai TS, Schram AM, Bielski CM, Donoghue MTA, Jonsson P, et al. Accelerating Discovery of Functional Mutant Alleles in Cancer. *Cancer discovery*. 2018;8(2):174-83.
27. Toy W, Shen Y, Won H, Green B, Sakr RA, Will M, et al. ESR1 ligand-binding domain mutations in hormone-resistant breast cancer. *Nat Genet*. 2013;45(12):1439-45.
28. Bertucci F, Ng CKY, Patsouris A, Droin N, Piscuoglio S, Carbuccion N, et al. Genomic characterization of metastatic breast cancers. *Nature*. 2019;569(7757):560-4.
29. Bielski CM, Donoghue MTA, Gadiya M, Hanrahan AJ, Won HH, Chang MT, et al. Widespread Selection for Oncogenic Mutant Allele Imbalance in Cancer. *Cancer cell*. 2018;34(5):852-62 e4.
30. Lee SC, North K, Kim E, Jang E, Obeng E, Lu SX, et al. Synthetic Lethal and Convergent Biological Effects of Cancer-Associated Spliceosomal Gene Mutations. *Cancer Cell*. 2018;34(2):225-41 e8.
31. Zhou Q, Derti A, Ruddy D, Rakiec D, Kao I, Lira M, et al. A chemical genetics approach for the functional assessment of novel cancer genes. *Cancer research*. 2015;75(10):1949-58.
32. Obeng E, McConkey, ME, Campagna, D, Schneider, RK, Chen, MC, Schmidt, PJ, Mullally, A, Fleming, MD, and Ebert, BL. Mutant Splicing Factor 3b Subunit 1 (SF3B1) Causes Dysregulated Erythropoiesis and a Stem Cell Disadvantage *Blood (ASH Abstract 828; 56th Annual American Society of Hematology meeting)*. 2014;124.
33. Adams JR, Xu K, Liu JC, Agamez NM, Loch AJ, Wong RG, et al. Cooperation between Pik3ca and p53 mutations in mouse mammary tumor formation. *Cancer research*. 2011;71(7):2706-17.
34. Yin S, Gambe RG, Sun J, Martinez AZ, Cartun ZJ, Regis FFD, et al. A Murine Model of Chronic Lymphocytic Leukemia Based on B Cell-Restricted Expression of Sf3b1 Mutation and Atm Deletion. *Cancer Cell*. 2019;35(2):283-96 e5.
35. Liu Z, Yoshimi A, Wang J, Cho H, Chun-Wei Lee S, Ki M, et al. Mutations in the RNA Splicing Factor SF3B1 Promote Tumorigenesis through MYC Stabilization. *Cancer Discov*. 2020;10(6):806-21.
36. Koren S, Reavie L, Couto JP, De Silva D, Stadler MB, Roloff T, et al. PIK3CA(H1047R) induces multipotency and multi-lineage mammary tumours. *Nature*. 2015;525(7567):114-8.
37. Wagner KU, Wall RJ, St-Onge L, Gruss P, Wynshaw-Boris A, Garrett L, et al. Cre-mediated gene deletion in the mammary gland. *Nucleic Acids Res*. 1997;25(21):4323-30.
38. Darman RB, Seiler M, Agrawal AA, Lim KH, Peng S, Aird D, et al. Cancer-Associated SF3B1 Hotspot Mutations Induce Cryptic 3' Splice Site Selection through Use of a Different Branch Point. *Cell reports*. 2015;13(5):1033-45.
39. Sato S, Sanjo H, Takeda K, Ninomiya-Tsuji J, Yamamoto M, Kawai T, et al. Essential function for the kinase TAK1 in innate and adaptive immune responses. *Nat Immunol*. 2005;6(11):1087-95.
40. Singh A, Sweeney MF, Yu M, Burger A, Greninger P, Benes C, et al. TAK1 inhibition promotes apoptosis in KRAS-dependent colon cancers. *Cell*. 2012;148(4):639-50.

41. Ajibade AA, Wang Q, Cui J, Zou J, Xia X, Wang M, et al. TAK1 negatively regulates NF-kappaB and p38 MAP kinase activation in Gr-1+CD11b+ neutrophils. *Immunity*. 2012;36(1):43-54.
42. Wu J, Powell F, Larsen NA, Lai Z, Byth KF, Read J, et al. Mechanism and in vitro pharmacology of TAK1 inhibition by (5Z)-7-Oxozeaenol. *ACS chemical biology*. 2013;8(3):643-50.
43. Helbig G, Christopherson KW, 2nd, Bhat-Nakshatri P, Kumar S, Kishimoto H, Miller KD, et al. NF-kappaB promotes breast cancer cell migration and metastasis by inducing the expression of the chemokine receptor CXCR4. *The Journal of biological chemistry*. 2003;278(24):21631-8.
44. Sovak MA, Bellas RE, Kim DW, Zanieski GJ, Rogers AE, Traish AM, et al. Aberrant nuclear factor-kappaB/Rel expression and the pathogenesis of breast cancer. *J Clin Invest*. 1997;100(12):2952-60.
45. Cogswell PC, Guttridge DC, Funkhouser WK, and Baldwin AS, Jr. Selective activation of NF-kappa B subunits in human breast cancer: potential roles for NF-kappa B2/p52 and for Bcl-3. *Oncogene*. 2000;19(9):1123-31.
46. Slamon DJ, Leyland-Jones B, Shak S, Fuchs H, Paton V, Bajamonde A, et al. Use of chemotherapy plus a monoclonal antibody against HER2 for metastatic breast cancer that overexpresses HER2. *N Engl J Med*. 2001;344(11):783-92.
47. Baselga J, Cortes J, Kim SB, Im SA, Hegg R, Im YH, et al. Pertuzumab plus trastuzumab plus docetaxel for metastatic breast cancer. *N Engl J Med*. 2012;366(2):109-19.
48. Andre F, Ciruelos E, Rubovszky G, Campone M, Loibl S, Rugo HS, et al. Alpelisib for PIK3CA-Mutated, Hormone Receptor-Positive Advanced Breast Cancer. *N Engl J Med*. 2019;380(20):1929-40.
49. Baselga J, Campone M, Piccart M, Burris HA, 3rd, Rugo HS, Sahmoud T, et al. Everolimus in postmenopausal hormone-receptor-positive advanced breast cancer. *N Engl J Med*. 2012;366(6):520-9.
50. Finn RS, Martin M, Rugo HS, Jones S, Im SA, Gelmon K, et al. Palbociclib and Letrozole in Advanced Breast Cancer. *N Engl J Med*. 2016;375(20):1925-36.
51. Ciriello G, Gatza ML, Beck AH, Wilkerson MD, Rhie SK, Pastore A, et al. Comprehensive Molecular Portraits of Invasive Lobular Breast Cancer. *Cell*. 2015;163(2):506-19.
52. Chang MT, Asthana S, Gao SP, Lee BH, Chapman JS, Kandoth C, et al. Identifying recurrent mutations in cancer reveals widespread lineage diversity and mutational specificity. *Nature biotechnology*. 2016;34(2):155-63.
53. Le DT, Uram JN, Wang H, Bartlett BR, Kemberling H, Eyring AD, et al. PD-1 Blockade in Tumors with Mismatch-Repair Deficiency. *N Engl J Med*. 2015;372(26):2509-20.
54. Robson M, Im SA, Senkus E, Xu B, Domchek SM, Masuda N, et al. Olaparib for Metastatic Breast Cancer in Patients with a Germline BRCA Mutation. *N Engl J Med*. 2017;377(6):523-33.
55. Lehmann BD, Bauer JA, Chen X, Sanders ME, Chakravarthy AB, Shyr Y, et al. Identification of human triple-negative breast cancer subtypes and preclinical models for selection of targeted therapies. *J Clin Invest*. 2011;121(7):2750-67.
56. Gucalp A, Tolaney S, Isakoff SJ, Ingle JN, Liu MC, Carey LA, et al. Phase II trial of bicalutamide in patients with androgen receptor-positive, estrogen receptor-negative metastatic Breast Cancer. *Clin Cancer Res*. 2013;19(19):5505-12.
57. Inoue D, Chew GL, Liu B, Michel BC, Pangallo J, D'Avino AR, et al. Spliceosomal disruption of the non-canonical BAF complex in cancer. *Nature*. 2019.
58. Chandralapaty S. Negative feedback and adaptive resistance to the targeted therapy of cancer. *Cancer discovery*. 2012;2(4):311-9.
59. Vasan N, Razavi P, Johnson JL, Shao H, Shah H, Antoine A, et al. Double PIK3CA mutations in cis increase oncogenicity and sensitivity to PI3Kalpha inhibitors. *Science*. 2019;366(6466):714-23.
60. Plante I, Stewart MK, and Laird DW. Evaluation of mammary gland development and function in mouse models. *J Vis Exp*. 2011(53).
61. Stanko JP, and Fenton SE. Quantifying Branching Density in Rat Mammary Gland Whole-mounts Using the Sholl Analysis Method. *J Vis Exp*. 2017(125).

62. Bankhead P, Loughrey MB, Fernandez JA, Dombrowski Y, McArt DG, Dunne PD, et al. QuPath: Open source software for digital pathology image analysis. *Sci Rep.* 2017;7(1):16878.
63. Li Z, Razavi P, Li Q, Toy W, Liu B, Ping C, et al. Loss of the FAT1 Tumor Suppressor Promotes Resistance to CDK4/6 Inhibitors via the Hippo Pathway. *Cancer Cell.* 2018;34(6):893-905 e8.
64. Subramanian A, Tamayo P, Mootha VK, Mukherjee S, Ebert BL, Gillette MA, et al. Gene set enrichment analysis: a knowledge-based approach for interpreting genome-wide expression profiles. *Proc Natl Acad Sci U S A.* 2005;102(43):15545-50.
65. Liao Y, Smyth GK, and Shi W. featureCounts: an efficient general purpose program for assigning sequence reads to genomic features. *Bioinformatics.* 2014;30(7):923-30.
66. Love MI, Huber W, and Anders S. Moderated estimation of fold change and dispersion for RNA-seq data with DESeq2. *Genome biology.* 2014;15(12):550.
67. Pereira B, Chin SF, Rueda OM, Vollan HK, Provenzano E, Bardwell HA, et al. The somatic mutation profiles of 2,433 breast cancers refines their genomic and transcriptomic landscapes. *Nat Commun.* 2016;7:11479.

Supplemental Tables

Table S1. Raw input of genomic alteration data to generate Figure 1A (<https://www.cbioportal.org/oncoprinter>).

Table S2. Raw input of clinical data to generate Figure 1A (<https://www.cbioportal.org/oncoprinter>).

Table S3. Pan-cancer SF3B1 mutated samples used for unsupervised clustering in Figure 3A.

Table S4. Genes with a differentially spliced cryptic 3'ss that also get differentially expressed between SF3B1 mutants and wild-types on MSK breast cancer cell lines. Related to Figure 4E.

Table S5. Genes with a differentially spliced cryptic 3'ss that also get differentially expressed between SF3B1 mutants and wild-types on TCGA breast cancer dataset. Related to Figure 4E.

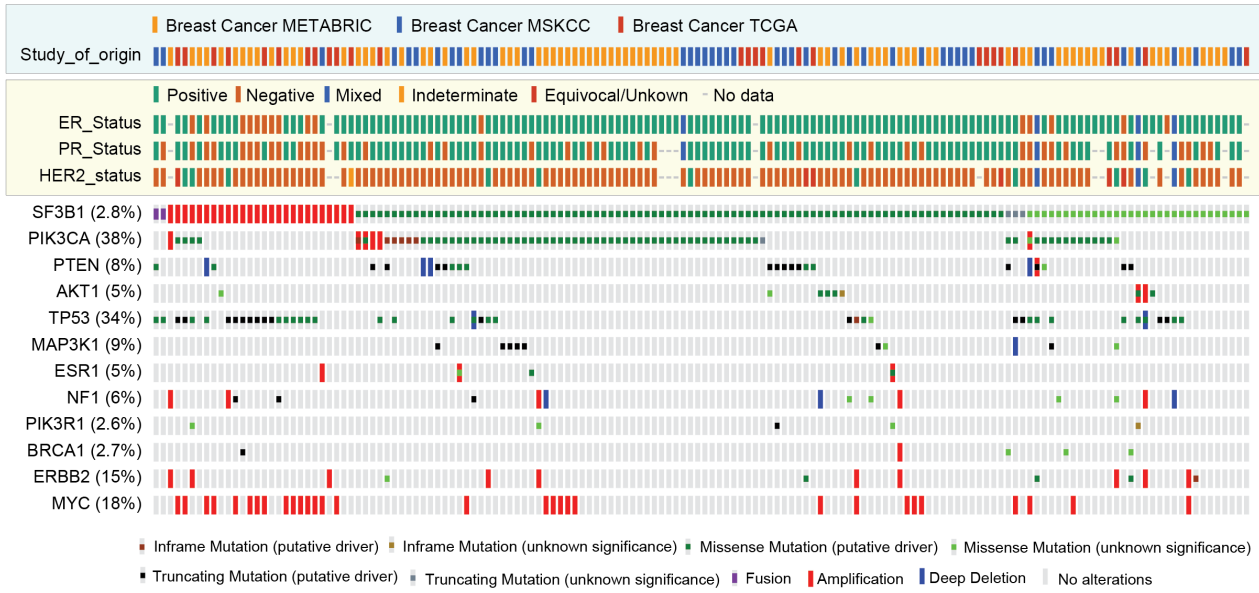
Table S6. Genes with a differentially spliced cryptic 3'ss between SF3B1 mutants and wild-types on MSK Mouse model RNASeq. Related to Figure 4E.

Table S7. Antibodies used in this study.

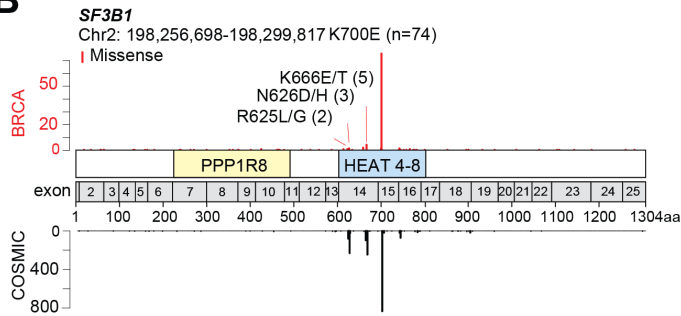
Table S8. Oligonucleotides used in this study.

Figure 1

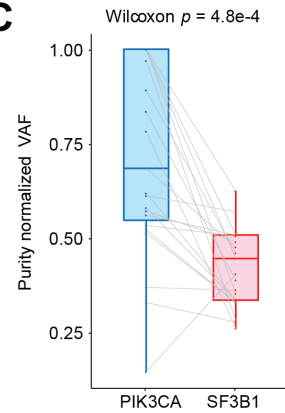
A



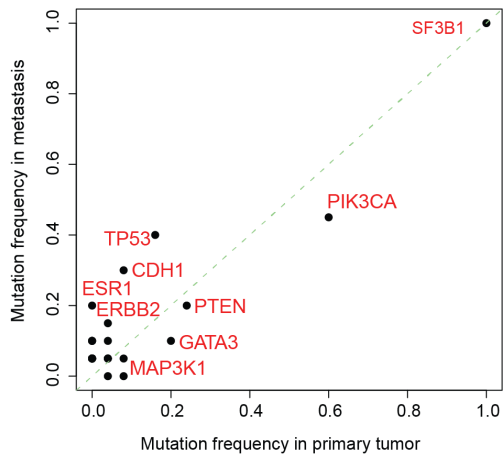
B



C



D



E

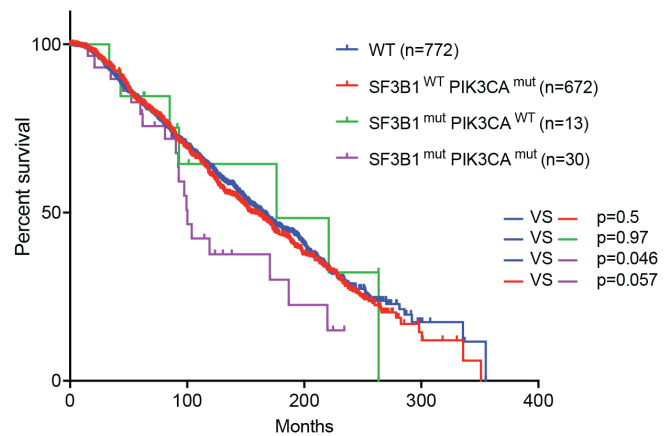


Figure 1. *SF3B1* hotspot mutations are recurrent in breast cancer and significantly associated with mutations activating PI3K signaling and shortened survival. (A) Oncoprint of somatic alternations in *SF3B1* and other breast cancer drivers across 5,366 patients from the METABRIC (24, 67), MSK-IMPACT (25), and TCGA (23) breast cancer cohorts. ER: estrogen receptor; PR: progesterone receptor; HER2: human epidermal growth factor receptor 2. (B) *SF3B1* mutation maps showing the counts, amino acid change, position, and evidence of mutational hotspots, based on COSMIC database information. Y axis counts at the bottom of the maps reflect the number of identified mutations in the COSMIC database. (C) Purity normalized variant allele frequency (VAF) of *PIK3CA* and *SF3B1* mutations amongst 51 double mutated samples in MSK-IMPACT cohort. (D) Frequency of somatic mutations in MSK-IMPACT patients ($n = 94$) harboring *SF3B1* hotspot mutations. Mutation frequency was calculated for each reported gene in $n = 57$ primary samples (x-axis) and $n = 45$ metastasis samples (y-axis), respectively. (E) Kaplan-Meier curve of disease-free survival in *SF3B1* hotspot mutant ($n=13$), *SF3B1* wild-type *PIK3CA* mutant ($n=672$), and *SF3B1/PIK3CA* double mutant ($n=30$) versus wild-type (WT, $n=772$) ER-positive breast cancer patients from METABRIC. P values were derived from log-rank test. See also Figure S1.

Figure 2

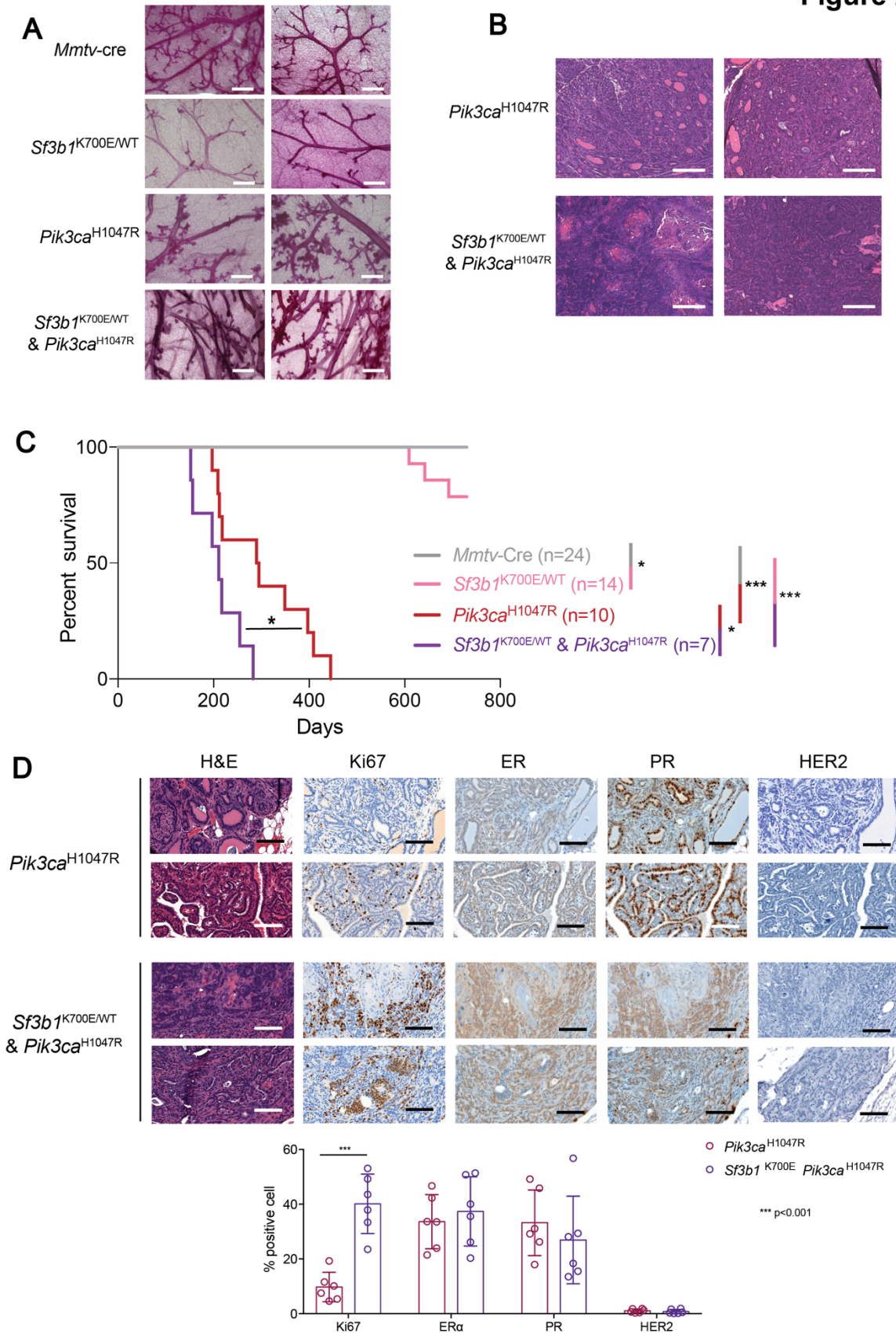
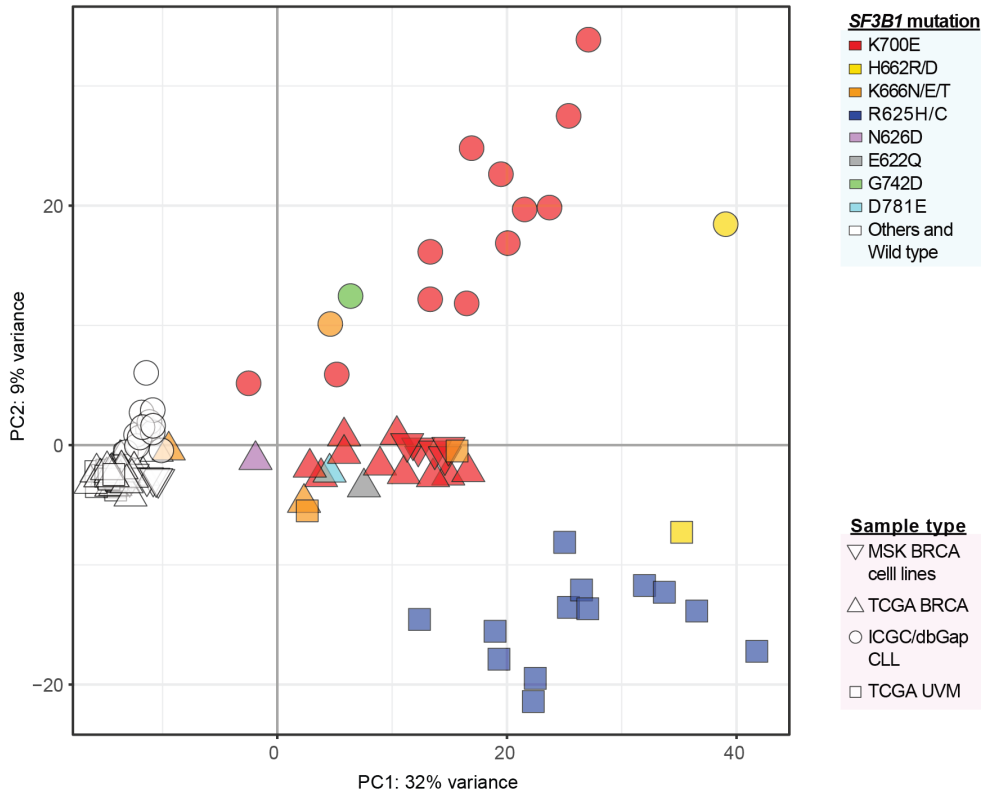


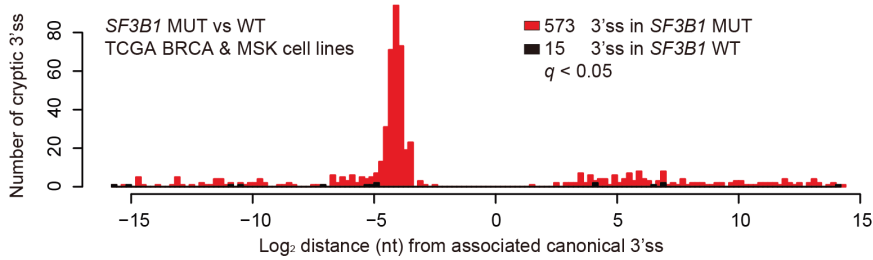
Figure 2. *Sf3b1*^{K700E} mutation promote mammary tumorigenesis in conjunction with mutant *Pik3ca*. (A) Whole-mount hematoxylin-staining of mammary glands from *MMTV-cre* control, *MMTV-cre Sf3b1*^{K700E/WT}, *MMTV-cre R26-LSL-Pik3ca*^{H1047R} and *MMTV-cre Sf3b1*^{K700E/WT} *R26-LSL-Pik3ca*^{H1047R} at the age of 4 months. Two representative examples are shown. Bar, 500 μ M. (B) Representative sections of hematoxylin and eosin (H&E) stained mammary glands from the mice in (A) at time of death. Two representative examples are shown. Scale bar: 250 μ M. (C) Kaplan-Meier survival curve of the mice from (A). The endpoint criterion was presence of tumors ≥ 1 cm³. P values calculated by Log-rank (Mantel-Cox) test in Prism 7 software. (D) H&E and immunohistochemical staining of breast tumors developing in *MMTV-cre R26-LSL-Pik3ca*^{H1047R} transgenic and compound *Sf3b1*^{K700E/WT} *Pik3ca*^{H1047R} transgenic mice. ER: estrogen receptor; PR: progesterone receptor. Scale bar: 100 μ M. Quantitation of percentage of positively stained cells (n=6 tumors/group) is shown below. *** p<0.001 (Student's t test). See also Figure S2-4.

Figure 3

A



B



C

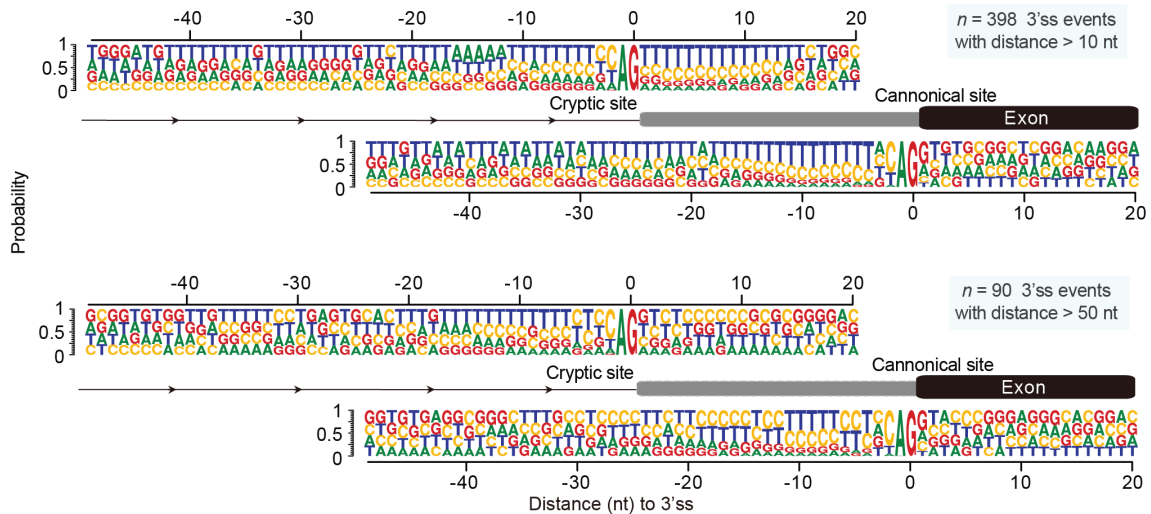


Figure 3. Differential aberrant 3' splicing events across *SF3B1* mutant cancers. **(A)** Principal component analysis of differential 3' splice sites (3'ss) in *SF3B1* mutant and wild-type samples. The input PSI matrix contains 618 cryptic 3'ss events identified from the pan-cancer dataset are shown. BRCA: breast cancer; CLL; chronic lymphocytic leukemia; UVM: uveal melanoma. **(B)** Histogram of statistically significant ($q < 0.05$) cryptic 3' ss identified in BRCA samples WT (black) versus mutant (red) for *SF3B1* and their distance in nucleotides (nt) from the associated canonical 3' ss. **(C)** Consensus 3'ss motif near the associated cryptic 3' AG dinucleotide (top) and canonical 3' AG dinucleotide (bottom) for 398 aberrant 3'ss events >10 nt from the canonical 3' ss as well as 90 aberrant 3'ss events >50 nt from the canonical 3' ss. See also Figure S5-6.

Figure 4

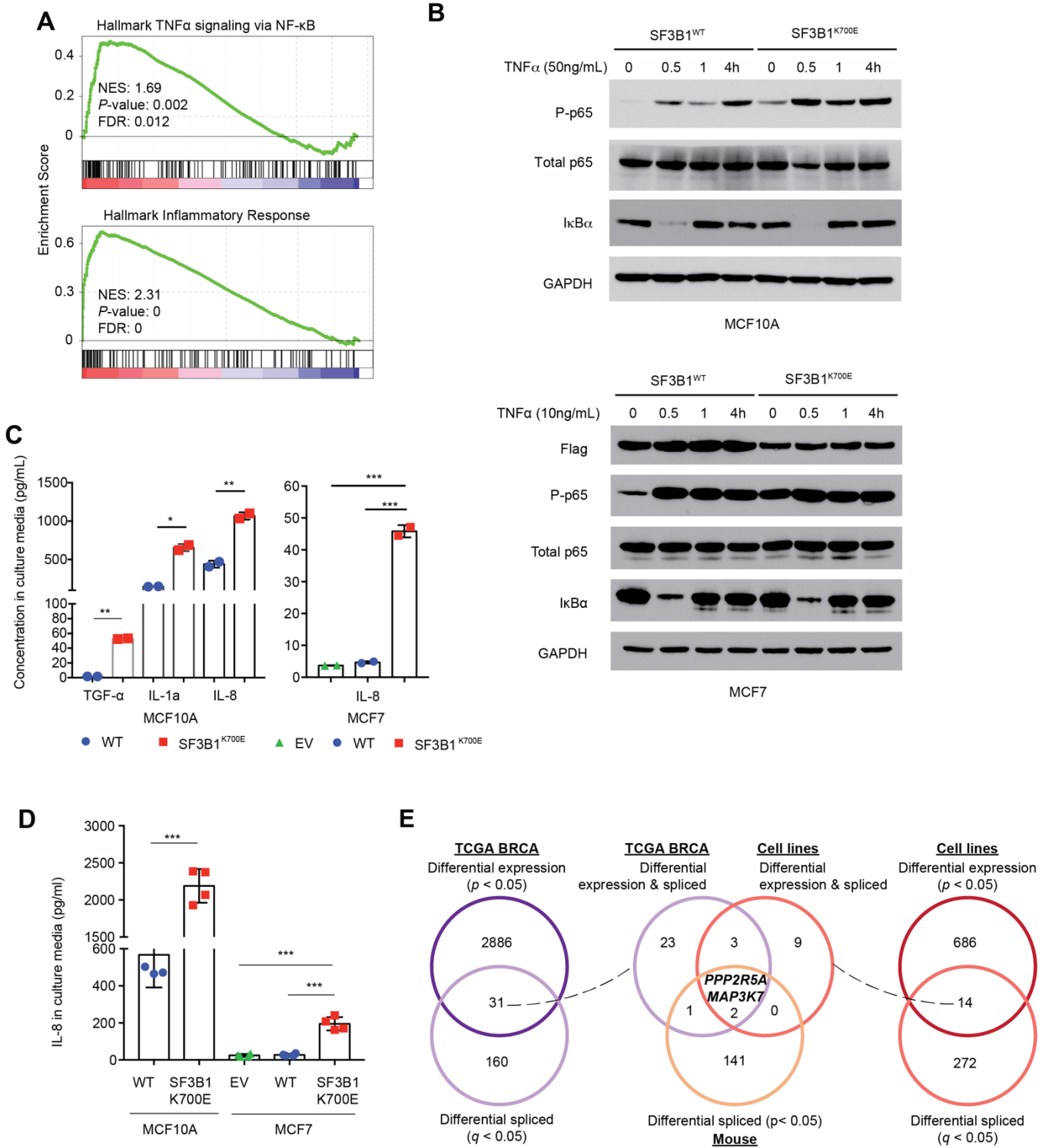


Figure 4. Increased inflammation and activation of NF- κ B signaling in *SF3B1*-mutant mouse and human breast tumors. (A) Gene set enrichment analysis identifies enrichment of hallmark gene sets of TNF α signaling via NF- κ B (top) and inflammatory response (bottom) in *SF3B1* mutant versus wild-type human breast cell lines. FDR: false discovery rate; NES: normalized enrichment score. **(B)** Activation of phospho-p65 (P-p65) upon TNF α stimulation of MCF10A *SF3B1*^{K700E/WT} mutant knockin cells (top) and MCF7 with transgenic expression of *SF3B1*^{K700E} versus *SF3B1*^{WT} cDNA (bottom). Quantitation of three independent experiments is shown in Figure S7B. **(C)** Levels of TGF α , IL-1a, and IL-8 in culture media from MCF10A cells from (B) or IL-8 in culture media from MCF7 cells with expression of an empty vector (EV), *SF3B1* WT, or *SF3B1* K700E cDNAs measured by Milliplex cytokine/chemokine multiplex assay. **(D)** Levels of IL-8 in culture media from (C) measured by ELISA. Mean levels with standard deviation shown. (*p<0.05, **p<0.01, ***p<0.0001; Student's t-test for MCF10A and Dunnett's multiple comparisons test for MCF7). **(E)** Venn diagrams of genes significantly differentially expressed (p <0.05; DESeq2) and spliced (q <0.05; t-test) across *SF3B1* mutant versus wild-type human breast cancers from TCGA (23) (left), isogenic human breast cell lines (right), and overlapping across human tumors, human cell lines, and mouse mammary epithelial cells mutant for *Sf3b1* (middle). See also Figure S7.

Figure 5

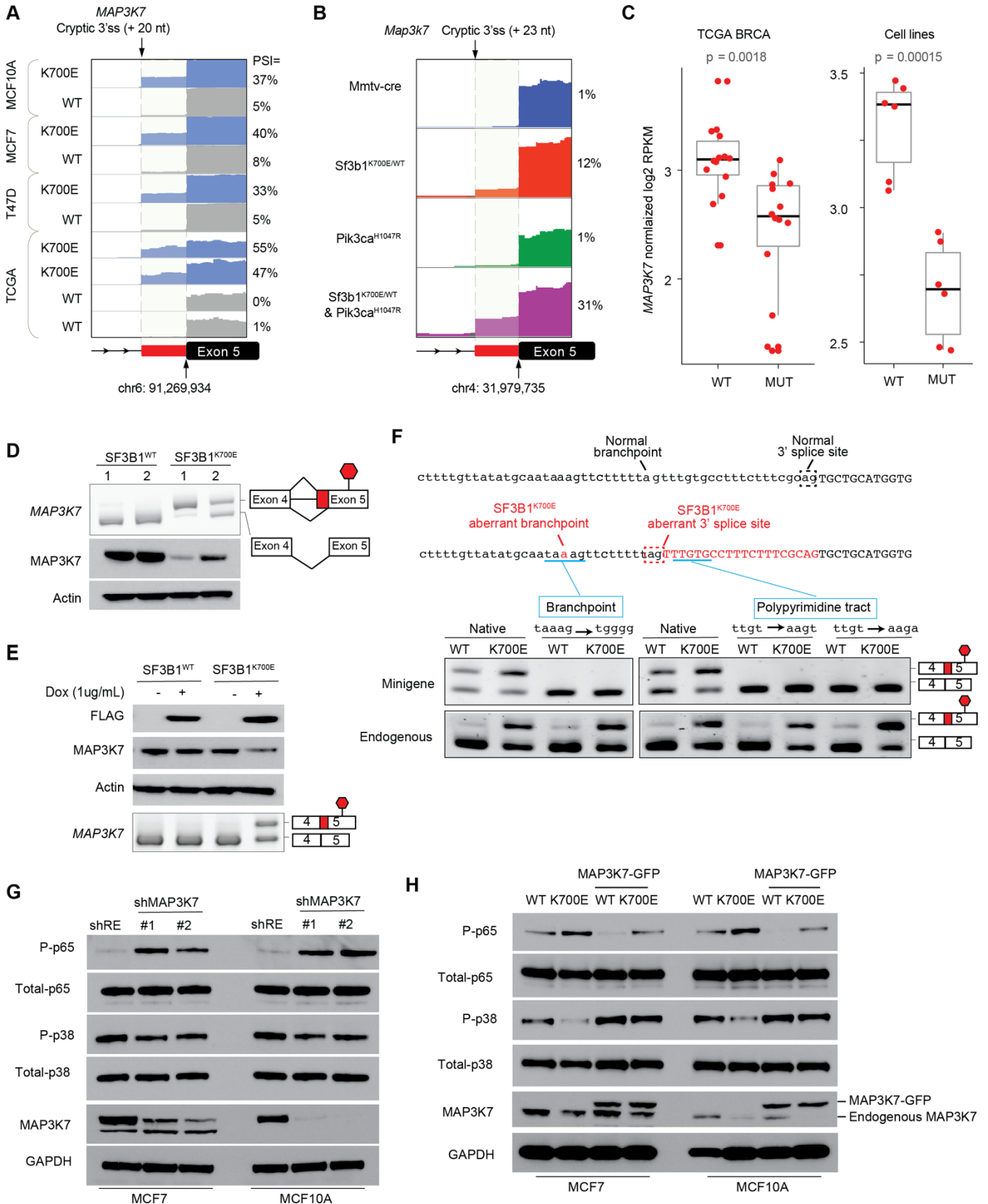


Figure 5. Aberrant splicing and downregulation of MAP3K7 by mutant SF3B1 promotes NF- κ B activation in breast cancer. Representative RNA-seq coverage plots showing cryptic 3' splice site (3' ss) usage in *MAP3K7* in (A) human isogenic breast cancer cell lines (MCF10A, MCF7, T47D) expressing wild-type ("WT") or SF3B1 K700E ("K700E") and human breast tumor samples from TCGA (23) as well as (B) mouse mammary epithelial cells from *MMTV-cre* control, *MMTV-cre Sf3b1^{K700E/WT}*, *MMTV-cre R26-LSL-Pik3ca^{H1047R}* transgenic, and compound *MMTV-cre Sf3b1^{K700E/WT} R26-LSL-Pik3ca^{H1047R}* mice. Percent Spliced In (PSI) value is shown on right of each coverage plot. (C) *MAP3K7* mRNA expression (normalized log₂RPKM values) in *SF3B1* mutant ("MUT") versus WT human breast tumors from TCGA and cell lines from (A). Box indicates upper and lower quartiles; thick bar indicates the median value. Whiskers indicate the largest/smallest value no further than 1.5 times the inter-quartile range. (D) RT-PCR of *MAP3K7* splicing event (top) and *MAP3K7* protein levels in isogenic MCF10A cells with or without *SF3B1^{K700E}* knockin. 3'ss utilized is shown in the schematic. (E) *MAP3K7* protein levels in MCF7 cells expressing doxycycline-inducible FLAG-SF3B1^{WT} or FLAG-SF3B1^{K700E} vectors. RT-PCR of *MAP3K7* splicing is shown on bottom. (F) RT-PCR of *MAP3K7* splicing event derived from *MAP3K7* minigene with mutations at aberrant branchpoint or polypyrimidine region downstream the aberrant 3'ss. RT-PCR of *MAP3K7* splicing event derived from endogenous *MAP3K7* is shown on bottom. A schematic of sequences around the normal and aberrant branchpoint and splice site is shown on top. (G) *MAP3K7* and phospho- and total p65 and p38 levels in MCF7 and MCF10A cells transduced with anti-*MAP3K7* shRNA. (H) *MAP3K7* and phospho- and total p65 and p38 levels in MCF7 and MCF10A cells expressing SF3B1 K700E mutant from (D) and (E) transduced with or without *MAP3K7-GFP* cDNA. Quantitation of three independent experiments is shown in Figure S8. See also Figures S8-9.

Figure 6

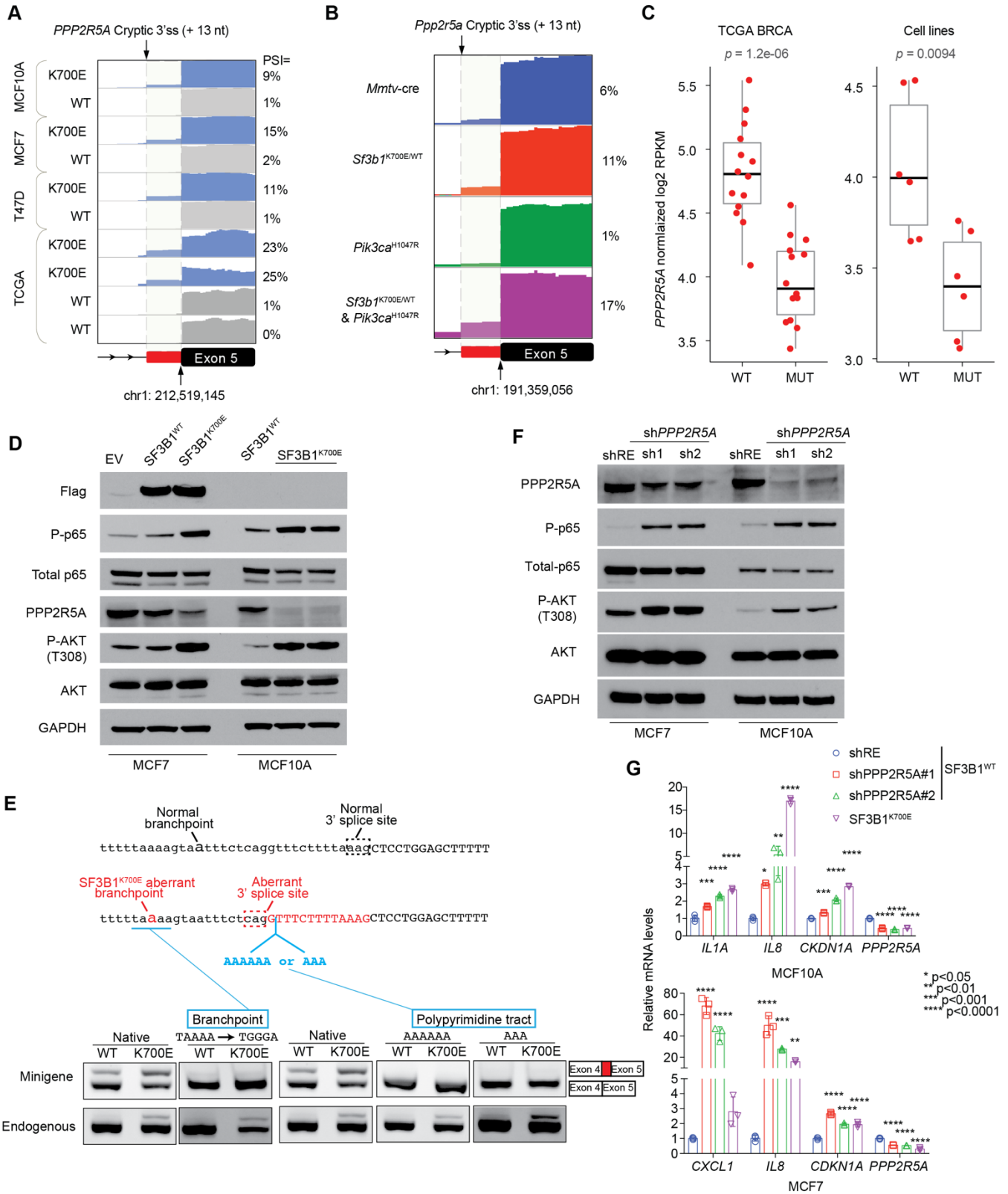


Figure 6. Aberrant splicing and downregulation of PPP2R5A by mutant SF3B1 promotes AKT activation and inflammatory signaling in breast cancer. Representative RNA-seq coverage plots showing cryptic 3' splice site (3'ss) usage in *PPP2R5A* in **(A)** human isogenic breast cancer cell lines (MCF10A, MCF7, T47D) expressing wild-type ("WT") or SF3B1 K700E ("K700E") and human breast tumor samples from TCGA (23) as well as **(B)** mouse mammary epithelial cells from *MMTV-cre* control, *MMTV-cre Sf3b1^{K700E/WT}*, *MMTV-cre R26-LSL-Pik3ca^{H1047R}* transgenic, and compound *MMTV-cre Sf3b1^{K700E/WT} R26-LSL-Pik3ca^{H1047R}* mice. Percent Spliced In (PSI) value of each event is shown on right of each coverage plot. **(C)** *PPP2R5A* mRNA expression (normalized log₂RPKM values) in SF3B1 mutant ("MUT") versus WT primary human breast tumors from TCGA and cell lines from (A). Box indicates upper and lower quartiles; thick bar indicates the median value. Whiskers indicate the largest/smallest value no further than 1.5 times the inter-quartile range. **(D)** *PPP2R5A*, phospho- and total AKT, and p65 levels in MCF7 and MCF10A with and without mutant SF3B1 expression (EV: empty vector). Quantitation of three independent experiments is shown in Figure S10A. **(E)** RT-PCR of *PPP2R5A* splicing event derived from *PPP2R5A* minigene with mutations at aberrant branchpoint or polypyrimidine region downstream the aberrant 3' splice site. RT-PCR of *PPP2R5A* splicing event derived from endogenous *PPP2R5A* is shown on bottom. A schematic of sequences around the normal and aberrant branchpoint and splice site is shown on top. **(F)** *PPP2R5A*, phospho- and total AKT, and p65 levels in MCF7 and MCF10A with and without *PPP2R5A* shRNA knockdown. Quantitation of three independent experiments is shown in Figure S10B. **(G)** Relative mRNA expression of *IL1A*, *CXCL1*, *IL8*, *CDKN1A*, and *PPP2R5A* in the cells from (D) and (F). Mean ± standard deviation shown; asterisks represent p values of Dunnett's test compared to sh*Renilla* control (shRE). See also Figure S9-10.

Figure 7

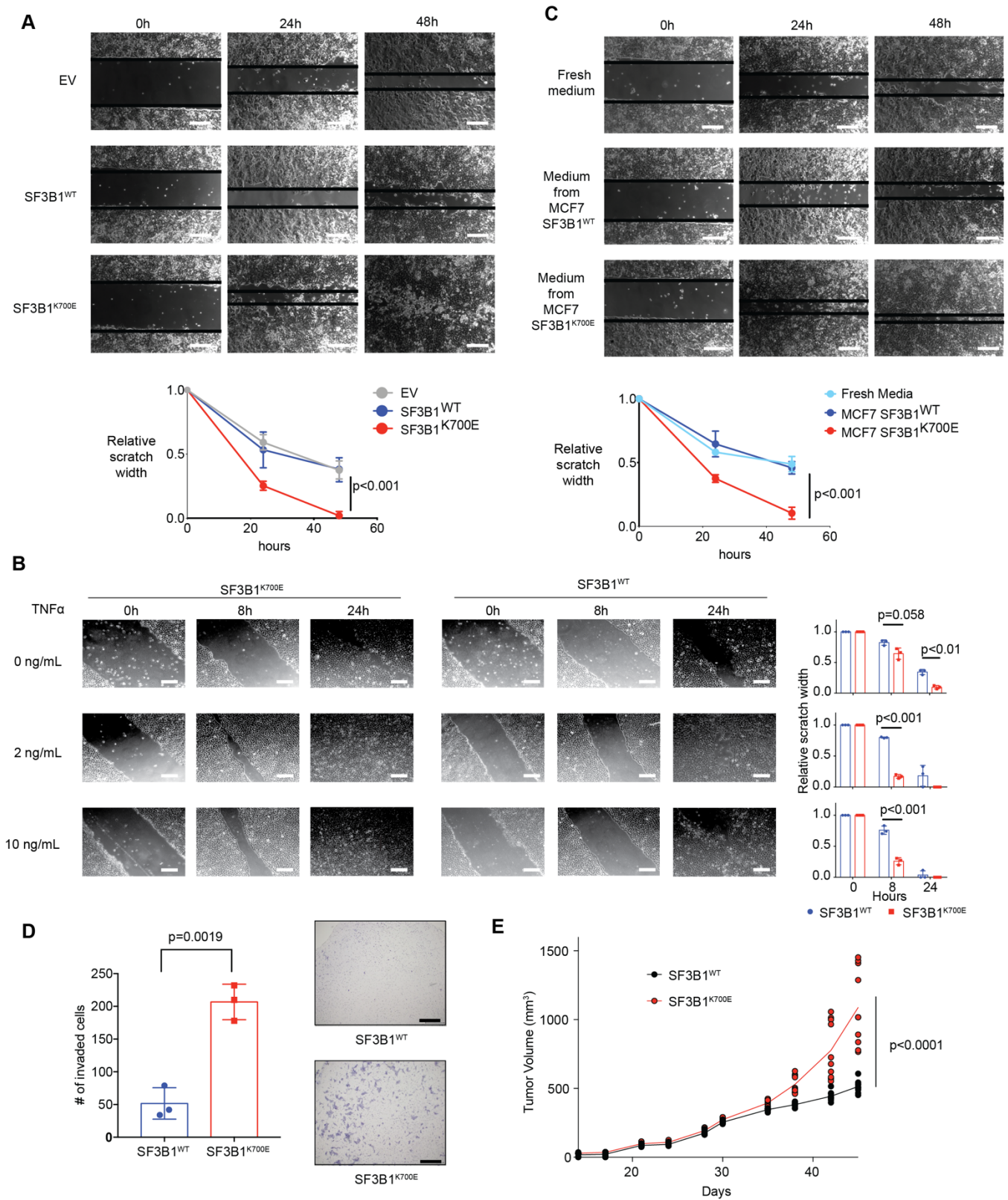


Figure 7. *SF3B1* mutations promote migration and invasion of breast cancer cells. (A)

Representative photos (top) at 0, 24, and 48 hours following wound creation in cell culture of MCF7 cells expressing an empty vector (EV), *SF3B1*^{WT}, or *SF3B1*^{K700E} cDNA. Scale bars represent 200 μ M. Relative scratch width over time shown below (n=3; mean value \pm standard deviation shown below; p values by ANOVA). **(B)** Quantification and representative photos (left) of wound at 0, 8, and 24 hours following wound creation and exposure to 0, 2, and 10ng/mL of TNF α in cell culture of MCF10A with or without knockin of *SF3B1*^{K700E}. Right, mean levels with standard deviation shown (n=3; p value by Student's test). Scale bars represent 500 μ M. **(C)** Same as (A) but for parental MCF7 cells exposed to medium from cells in (A). Scale bars represent 200 μ M. **(D)** Number of invaded MCF10A cells with or without knockin of *SF3B1*^{K700E} migrating towards epidermal growth factor (EGF) in a transwell invasion assay (left). Mean \pm standard deviation (n=3, p value by Student's t-test) shown. Right, photos of hematoxylin staining of the migrated cells (photos taken using a microscope with a 10x objective (total magnification 100x); scale bars represent 200 μ M). **(E)** Growth of MCF7 tumors expressing either wild-type or mutant *SF3B1* in NSG mice. Size of individual tumor (n=10 in each group) and the mean are shown (p value by ANOVA). See also Figure S11-12.

Figure 8

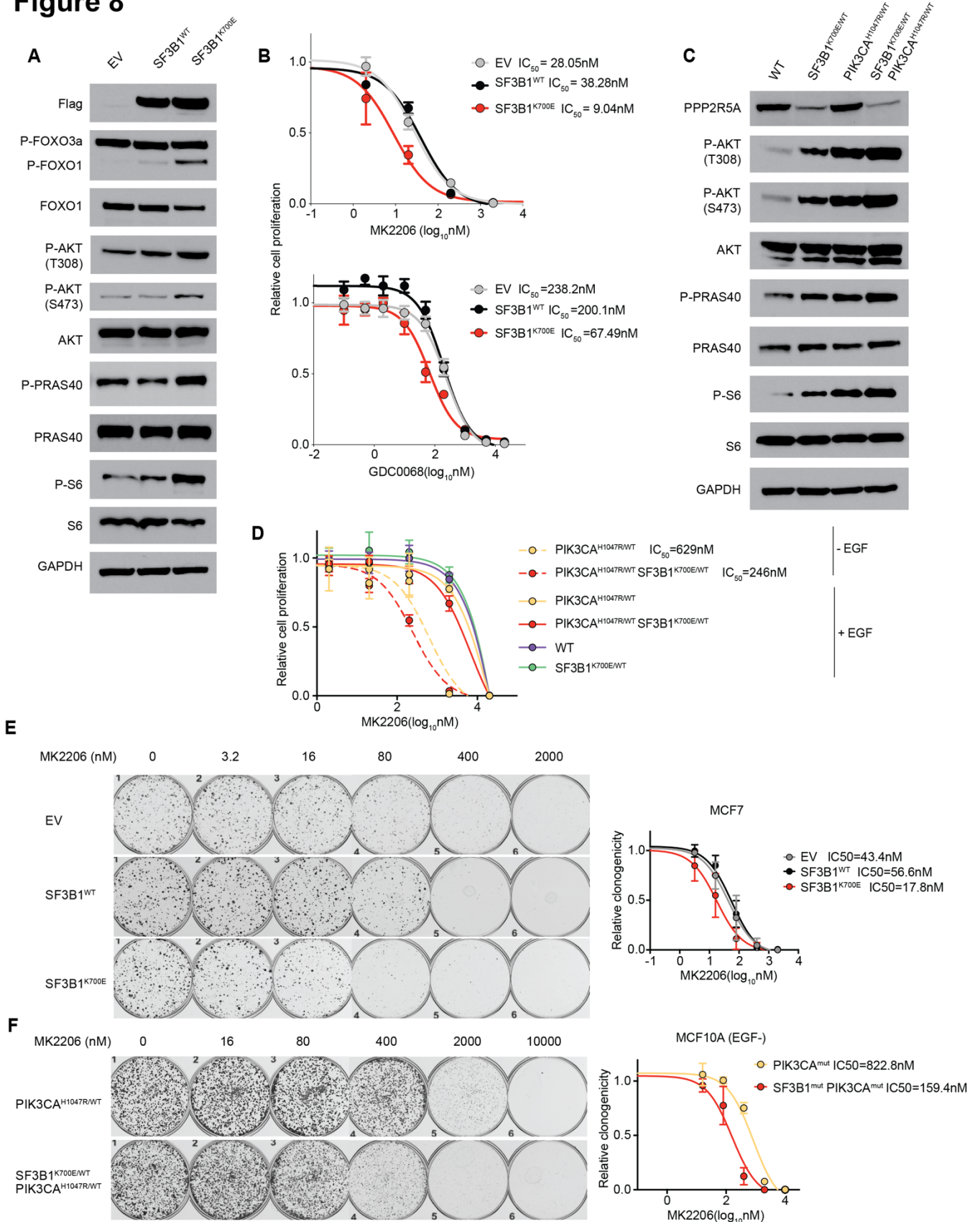


Figure 8. *SF3B1*^{K700E} mutation sensitizes breast cancer cells to AKT inhibitors. (A) Western blot of MCF7 cells expressing an empty vector (EV), *SF3B1* WT, or *SF3B1* K700E cDNA. **(B)** IC₅₀ of MCF7 cells from (A) following 5 days of exposure to MK2206 (left) or GDC0068 (right). Data are represented as means ± SD; n = 6. **(C)** Western blot of MCF10A WT cells as well as *SF3B1*^{K700E/WT} knockin cells, *PIK3CA*^{H1047R/WT} knockin cells and *SF3B1*^{K700E/WT} *PIK3CA*^{H1047R/WT} double knockin cells cultured in the absence of EGF. **(D)** IC₅₀ to MK2206 of MCF10A cells from (C) in the presence or absence of EGF (epidermal growth factor). Data are represented as means ± SD; n = 6. **(E)** Clonogenic survival assay of MCF7 cells from (A) following 21 days of exposure to MK2206. IC₅₀ curve is shown at right. **(F)** Clonogenic survival assay of MCF710A cells from (C) following 14 days of exposure to MK2206 in absence of EGF. IC₅₀ curve is shown at right. See also Figure S13-14.